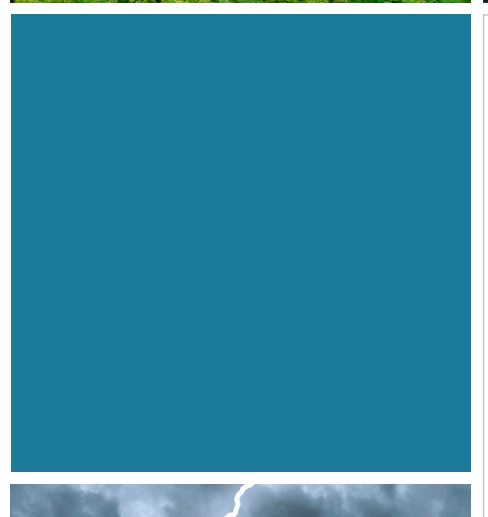
INCREASED FLEXIBILITY AND POWER PRODUCTION FROM BIOMASS THROUGH MATERIAL DEVELOPMENT AND CORROSION PREDICTION

RAPPORT 2023:932

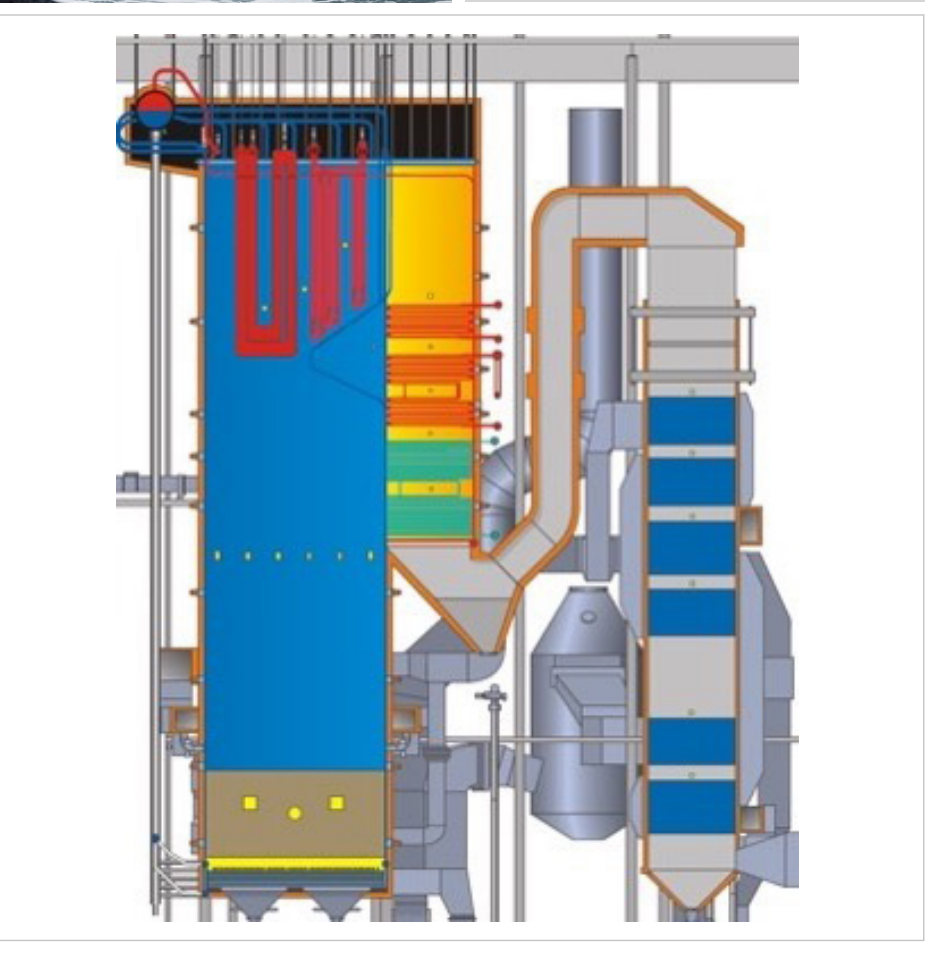














Increased flexibility and power production from biomass through material development and corrosion prediction

JOHAN EKLUND, JOHN HALD, RICHARD SHEN,
SØREN AAKJÆR JENSEN, HANNA KINNUNEN,
MARIA DOLORES PAZ OLAUSSON, LAURA RIOJA-MONLLOR,
VICENT SSENTEZA, BERTIL WAHLUND AND TORBJÖRN JONSSON

Foreword

The project has been performed within the framework of the materials technology research programme KME, Consortium materials technology for thermal energy processes, period 2018-2023. The consortium is at the forefront of developing material technology to create maximum efficiency for energy conversion of renewable fuels and waste.

KME was established 1997 and is a multi-cliental group of companies over the entire value chain, including stakeholders from the material producers, manufacturers of systems and components for energy conversion and energy industry (utilities), that are interested in materials technology research. The consortium is managed by Energiforsk.

The programme activities are characterized by long term industry and demand driven research and contribute to the development of thermal energy processes for efficient utilization of renewable fuels and waste in power and heat production. The KME goals are to bring about cost-effective materials solutions for increased availability and power production, improved fuel flexibility and improved operating flexibility, with low environmental impact.

With the goal to increase the efficiency and predictability/flexibility of power generation from biomass, the specific project has analyzed material development and oxidation simulations, through a combination of lab investigations, probe exposures as well as fixed installed material in a commercial boiler. Torbjörn Jonsson, Chalmers, has been the project leader, and Johan Eklund, Chalmers, main author. John Hald, DTU, Richard Shen, Kanthal, Søren Aakjær Jensen, Ørsted, Hanna Kinnunen, Valmet, Bertil Wahlund, Energiforsk, Laura Rioja-Monllor, Alleima, Johan Eklund, Maria Dolores Paz Olausson, Vicent Ssenteza and Torbjörn Jonsson, Chalmers, have been project participants and co-authors of the report. The industry has participated in the project through own investment (60 %) and the Swedish Energy Agency has financed the academic partners (40 %).

Energiforsk would like to thank all the participants for a well performed project.

Bertil Wahlund, Energiforsk

These are the results and conclusions of a project, which is part of a research programme run by Energiforsk. The authors are responsible for the content.



Summary

The overall aim of the project is to increase the efficiency and predictability/flexibility of power generation from biomass. In order to achieve this, two different pathways have been investigated, i.e., material development and oxidation simulations, through a combination of lab investigations, probe exposures as well as fixed installed material in a commercial boiler.

The laboratory studies showed that the none of the alloys resisted breakaway oxidation in the presence of KCl. However, minor additions of Si in the newly developed lean FeCrAl alloys were found to drastically reduce the oxide growth rate even after breakaway oxidation which provides the possibility to limit material degradation in harsh environments. The probe exposures, performed in two different boilers, showed that the chloride content was very low in both boilers and the exposed sample rings displayed negligent material loss after both the short-term exposure and the long-term exposure. The FeCrAl alloys generally performed best, especially at higher material temperature as they were able to retain the primary protection to a large extent. The thermally sprayed EF101M sample ring retained the primary protection (utilizing the oxidation prediction this would give a thickness of less than $2\mu m$ after 22000h at a material temperature of 700 °C) under all conditions which is promising for utilizing FeCrAl alloys without being limited by their pressure-bearing capabilities. The fixed installed test tubes installed in the tertiary superheater in the commercial boiler remained installed for approximately 22 000 hours. All test tubes (stainless steels) transitioned into the secondary corrosion regime during the operating lifetime. However, the material loss was minor for the long exposure duration. The results show the potential in material development/selection to increase the efficiency in power generation from biomass through higher material temperatures.

Thermodynamic/kinetic calculations were performed to investigate the possibility to provide predictions of the corrosion rates in laboratory - probe - fixed installed materials. The strategy was based on the formation or chromia, alumina and iron oxide with input from the literature/lab/probe/fixed installed samples to optimize and confirm the accuracy of the calculations. Given the mild boiler environment no large discrepancy between the corrosion rates in laboratory - probe - fixed installed materials could be observed. The strategy gave accurate calculated oxide thicknesses in some cases, while the inaccuracy in other cases offered insights into necessary future improvements of the model, taking into consideration the formation of a healing layer after breakaway oxidation. This new knowledge may in addition aid not only in better predictions but also to develop/select corrosion resistant materials for harsh environments showing the potential in corrosion simulations/lifetime predictions.

Keywords: Biomass-fired boiler, Superheater, FeCrAl, High temperature corrosion.



Sammanfattning

Det övergripande syftet med projektet är att öka effektiviteten och förutsägbarheten/flexibiliteten i el/värmeproduktion från biobränslen. För att uppnå målet har två strategier använts, dvs materialutveckling och oxidationstillväxtssimulering. Dessa parallella strategier har undersökts genom en kombination av laboratorieundersökningar, sondexponeringar samt fast installerat material i en kommersiell anläggning.

Laboratoriestudierna visade att ingen av legeringarna bildade/bibehöll en skyddande oxid (primärskyddet, dvs Cr2O3 eller Al2O3) i närvaro av KCl. Resultaten visade även att små tillsatser av Si i de nyutvecklade FeCrAllegeringarna drastiskt minskade oxidtillväxthastigheten efter nedbrytning av den skyddande oxiden vilket ger möjlighet att begränsa materialdegraderingen i mycket korrosiva miljöer som bio och avfallseldade kraftverk. Sondexponeringarna, utförda i två olika anläggningar, visade att kloridhalten var mycket låg i båda pannornas beläggningar och i linje med dessa resultat uppvisade de exponerade materialen försumbar materialförlust efter både korttidsexponeringen och långtidsexponeringen. FeCrAl-legeringarna presterade generellt bättre, speciellt vid högre materialtemperatur då de i stor utsträckning kunde behålla det primära skyddet. Den termiskt sprutade FeCrAl materialet EF101M behöll det primära skyddet (genom att använda oxidationssimulering kan detta beräknas motsvara en oxidtjocklek tunnare än 2µm efter 22 000h vid en materialtemperatur på 700 °C) under alla förhållanden, vilket är lovande för användning av FeCrAl-legeringar utan att begränsas av deras tryckbärande förmåga. De fast installerade provrören installerade i den tertiära överhettaren i den kommersiella pannan exponerades i cirka 22 000 timmar. Alla provrör (rostfria stål) övergick till den sekundära korrosionsregimen under drifttiden. Materialförlusten var dock liten under den långa exponeringstiden. Resultaten visar på potentialen i materialutveckling/materialval för att öka materialtemperaturen/effektiviteten vid kraftgenerering från biomassa.

Termodynamiska/kinetiska simuleringar utfördes för att undersöka möjligheten att prediktera korrosionshastigheterna i laboratorie - sond - fast installerade material. Strategin baserades på prediktering av kromoxid, aluminiumoxid och järnoxid med input från litteraturen/labbförsök/sondförsök/fast installerade prover för att optimera och verifiera simuleringarna. Med tanke på den milda pannmiljön kunde ingen stor avvikelse mellan korrosionshastigheterna i laboratorie - sond - fast installerade material observeras. De beräknade oxidtjocklekarna var korrekta för vissa fall, medan avvikelser i andra fall gav insikter i nödvändiga framtida förbättringar av modellen. Detta gäller speciellt med hänsyn till bildandet av ett skyddande skikt en tid efter den initiala skyddande oxiden brutits ned. Denna nya kunskap kan hjälpa till att förbättra modellerna för oxidationspredikteringar men även för att utveckla/välja korrosionsbeständiga material för tuffa miljöer. Detta visar den stora potentialen som korrosionssimuleringar/livstidsförutsägelser möjliggör.



List of content

1	Introd	luction		;	8
	1.1	Motiv	ation	:	٤
	1.2	Backg	round	9	_
	1.3	Goal o	of the project	10	
2	Descri	iption o	f the boilers	1:	
	2.1	Skærb	æk Boiler	1:	2
	2.2	Asnæs	s Boiler	1:	Ξ
3	Produ	ction of	f test material	14	/
	3.1	Sampl	e rings	14	′
		3.1.1	Commercial alloys	1	4
		3.1.2	Model alloys	1	4
		3.1.3	Kanthal® EF101	14	4
	3.2	Fixed i	installations	1	_
4	Experi	imental	procedure	1	E
	4.1	Lab ex	posures	1	E
		4.1.1	Sample preparation	1	E
		4.1.2	Exposures	1	E
		4.1.3	Analysis	1	,
	4.2	Probe	exposures	1	,
		4.2.1	Sample preparation	1	,
		4.2.2	Exposures	1	٤
		4.2.3	Analysis	1	٤
	4.3	Fixed i	installations	1	
		4.3.1	Exposures	1	
		4.3.2	Analysis	1	
	4.4	Experi	mental conditions in the boilers	20	(
		4.4.1	Fuel	20	(
		4.4.2	Fuel additives	2	
		4.4.3	Skærbæk (SKV402)	2	•
		4.4.4	Asnæs (ASV06)	2:	=
5	Oxida	tion sin	nulation	2	7
6	Result	ts and D	Discussion	2	
	6.1	Lab ex	posures	2:	0
	6.2	Probe	exposures	3:	:
	6.3	Fixed i	installations	4	•
	6.4	Oxidat	tion simulation	4	E
		6.4.1	The primary corrosion regime (Chromia/Alumina)	4	E
		6.4.2	The secondary corrosion regime (iron oxide)	4	c



7	Conclusions	52
8	Goal fulfilment	54
9	Suggestions for future work	56
10	References	57
11	Annendix	60



1 Introduction

1.1 MOTIVATION

Biomass is a resource which is carbon neutral and will play an important role in the transformation to an entirely renewable energy system. The use of biomass as fuel for power and combined heat and power (CHP) production has increased in the last decades. However, biomass contains aggressive alkali metals and chlorine which causes excessive boiler tube corrosion. This necessitates operation at relatively low steam temperatures compared to fossil fuels.

The relatively "benign" and well-defined biofuels such as forest residues are today operated with a steam data of max 540 °C. This may be compared to state-of-the-art fossil fuel plants with a substantially higher operating temperature (620 °C) and electric efficiency, i.e., there is a large potential given that the high temperature corrosion could be better controlled/predicted. Biofuel is today's dominant bioenergy source and an increase in steam temperature or better lifetime prediction would have a large impact on reliable operation, flexibility and reduce the overall costs of renewable energy from biomass by increasing efficiency and increasing/predicting materials lifetime.

The well-defined biofuels such as forest residues are characterized by higher levels of reactive alkali and lower levels of chlorine compared to recycled wood or waste. High temperature alloys that rely on protective oxide scales based on iron oxide and chromium oxide suffer rapid degradation in the superheater environment. Thus, the chromium oxide scales formed on e.g., stainless steels tend to be destroyed when exposed to alkali rich deposits. In contrast, aluminum oxide is relatively inert in contact with alkali at high temperature. This suggests that alloys forming alumina (Al₂O₃) as protective scales may be superior in the alkali rich fireside environment such as well-defined biofuels. This new class of materials could thereby improve the efficiency of biomass boilers through higher steam data/longer lifetime of key components.

In order to improve the flexibility of these processes the impact of temperature/environment on lifetime is a key issue. This is normally tested through laboratory - probe - fixed installed materials. However, there may be a large discrepancy between the corrosion rates. Thanks to the rapid developments in both modelling and characterization methods, reliable predictions of corrosion rates from fundamental thermodynamic data are now for the first time available. This may be implemented in order to better link the short time test to the long-time behavior, i.e., the lifetime predictions of key components such as superheaters. Improved upscaling of key test parameters may give a higher flexibility when assessing the corrosion process such that a faster materials selection process could be adopted to new challenges and increase the potential of biomass-fired power boilers.



1.2 BACKGROUND

Biomass as a resource

In order to reduce global warming, the electricity produced by clean energy sources such as wind, solar, and hydroelectric power is increasing. However, there will be a need for thermal power plants as a safety net to compensate for the fluctuations in electricity production, as the other sources depend on meteorological factors which cannot be controlled. Biomass for energy production may therefore play a very important role to reduce the amount of CO₂ emitted can be sequestered via photosynthesis in a much shorter period of time compared with fossil fuels such as coal. Thermal power plants can be controlled to run as the need arises, e.g., during the day with standby at night.

Fireside corrosion in biomass fired plants

In contrast to fossil fuels which contain high amounts of sulphur (oil) and/or alumina silicates (coal), biomass when combusted leads to release of KCl aerosols and HCl and SO2 as well as water vapour and carbon dioxide. KCl reacts with the SO₂ in the flue gas to result in sulphates. If the KCl aerosols are not neutralized in the combustion zone, these will condense as fly-ash onto vulnerable components such as superheaters and result in corrosion. The neutralization of the KCl can depend on the flue gas temperature where a lower temperature enhances sulphation due to the stability of SO3. Agricultural biomass such as straw results in thick KCl containing deposits, but even combustion of biofuels such as wood chip will lead to tenacious deposits containing both K2SO4 and KCl. These condensed KCl particles can be sulphated releasing Cl species that may attack the metallic tube or react directly with protective oxides such as Cr2O3 to form potassium chromates [1]. Plant data have shown that metal temperature is the primary parameter, but that flue gas temperature also influences corrosion rates as it results in higher surface metal temperatures but may also affect the sulphation of KCl and volatilization of metal chlorides. The flue gas temperature is also linked to the boiler type, fluidized bed vs grate firing and this aspect has previously not been part of a dedicated investigation in corrosion studies.

Material selection and development - Stainless steels and FeCrAl alloys and coatings

High temperature alloys that rely on protective oxide scales based on iron oxide and chromium oxide suffer rapid degradation in the superheater environment. Thus, the chromium oxide scales formed on e.g. stainless steels tend to be destroyed when exposed to alkali chloride deposits. However, there is a large difference between different alloys in lifetime even though they lose the protective Cr rich scale. The alloys would then rely on the secondary protection from other alloying elements and very little is known about how such elements influence the corrosion resistance of these alloys in this environment, see e.g. [2, 3]. Thermodynamic kinetic modelling may predict the impact of alloying elements on the secondary protection, see below.

In contrast to chromia, aluminum oxide is more inert in contact with alkali at high temperature. This suggests that alloys forming alumina (Al2O3) as protective scales



may be superior in the alkali rich fireside environment. Presently, alloys forming alumina scales are not used and commercial alumina formers are designed for use at temperatures higher than typical superheater temperatures. However, recent (unpublished) research implies that the corrosion properties of commercial FeCrAl alloys may be superior to the best NiCr-based alloys in biomass combustion environments. Since this class of materials has limited load bearing capacity at high temperatures and limited ductility at low temperature, they will likely be used as coatings or as the outer part of composite tubes. Ferritic and austenitic alumina forming alloys are being developed by Kanthal, one of participating company in this project. Kanthal has provided model alloy samples for testing.

Predicting component lifetime – state-of-the-art thermodynamic modelling

In an ideal world, accurate numerical models would exist for the oxidation process which are based upon the underlying thermodynamics and mass transport processes which are prevalent. A substantial progress in this regard has been made in recent years resulting in models with greater predictive power sensitive to the underlying alloy composition. The Calphad approach has been successfully applied in quantitative diffusion process simulations for a number of industrially important material systems, such as steels, superalloys, and aluminum alloys. Diffusion in oxides is more difficult and has been under development the last years and the first models for iron, chromium and aluminum oxides are now available, see e.g., [4, 5]. These models have in this project for the first time be implemented together with advanced characterization techniques in order to predict growth rates in laboratory scale, on probe samples exposed in boilers as well as on fixed installed material in a boiler. The modelling has been used to link the in-situ experiments with laboratory testing to be able to study/predict the impact of key variables such as temperature to the lifetime of the components and thereby create a more flexible system for the future.

1.3 GOAL OF THE PROJECT

The overall goal of the project is to increase the efficiency and flexibility/predictability of power generation from biomass. This will improve plant economy and the competitiveness of biomass.

The project results contributes to 2030 Swedish Energy Agency goals in the following way:

- Power generation from biomass contributes to a completely renewable and flexible electrical system by providing planned power generation. The scale up investigation of small scale tests enables faster development and a more flexible system in the future.
- Materials that allow higher steam data of conversion of biofuels to electricity and heat enables a resource-efficient and cost-effective manner with minimal environmental impact.
- The collaboration and continuous exchange of knowledge within the project includes the whole value chain. The research within the project has been in the research front implementing novel methods e.g. state of the art



thermodynamic modelling securing that Swedish research in this field continues to maintain a high international level.

The scientific goals of the project:

- Determine the applicability and limitations of aluminum oxide forming materials for improved biomass conversion effect, as well as their comparison with existing materials.
- Implement thermodynamic-kinetic modelling of oxidation in complex environments.
- Scale up lab-probe-fixed installation tests predict impact of e.g. material and temperature on lifetime of key components.

The research within the project is in the research front implementing novel methods as e.g. state-of-the-art thermodynamic modelling. The aim is to publish the work in scientific journals and produce PhD students within the project.

Academic goals of the project:

- Academic thesis two
- Journal publications two



2 Description of the boilers

Site activities within the project included Skærbæk Boiler 402 (SKV402) and Asnæs Boiler 6 (ASV06). Both are operated by Ørsted. Short facts for these boilers are given in the following sections.

2.1 SKÆRBÆK BOILER

Skærbæk Boiler 402 (SKV402) is located at the Skærbæk Power Station in Skærbæk, Denmark. It was manufactured by Babcock & Wilcox Vølund and is a grate-fired boiler (natural circulation drum-type). The first fire of the boiler started in May 2017. The boiler uses wood chips as fuel and has a nominal thermal heat input of 151 MJ/s (with steam pressure and temperature being 82 bar and 542 °C, respectively).

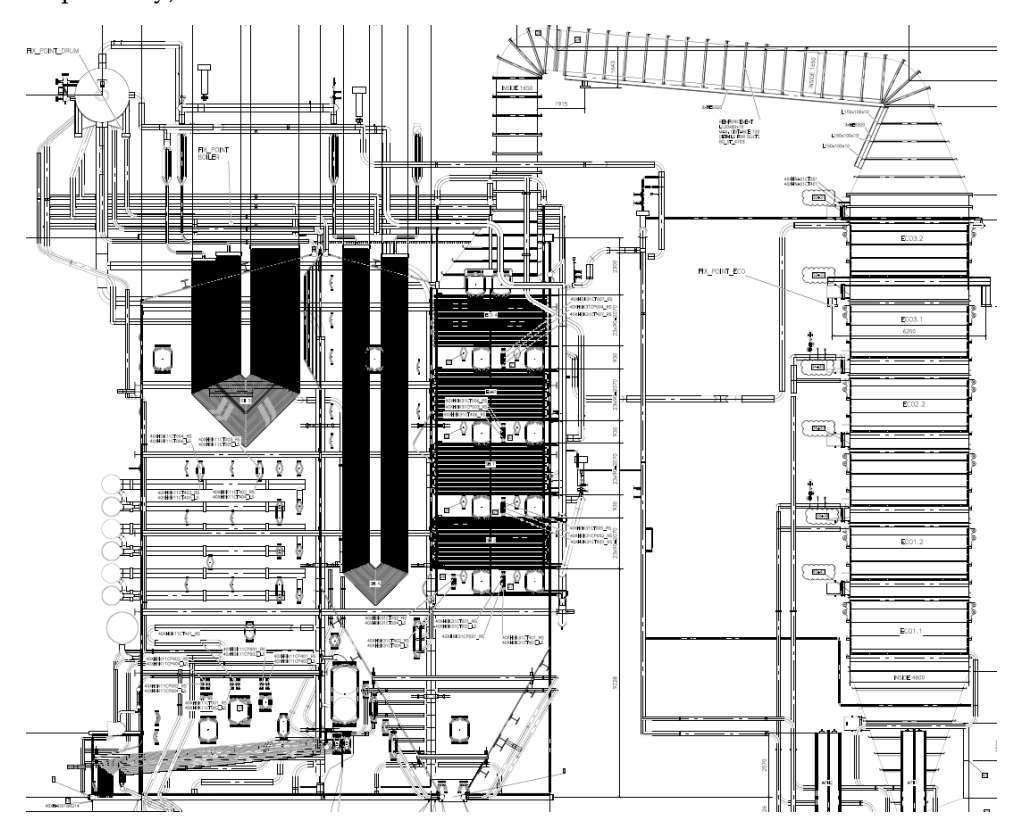


Figure 1: Schematic drawing of the SKV402 boiler.



2.2 ASNÆS BOILER

Asnæs Boiler 6 (ASV06) is located at the Asnæs power station in Kalundborg, Denmark. It was manufactured by Valmet and is a bubbling fluidized bed boiler (natural circulation drum type). The first fire started in June 2019, which marks the start of the exposure of the fixed installations. Similar to the SKV402 boiler, the ASV06 boiler uses wood chips as fuel and produces steam pressure and temperature of 100 bar and 540 °C respectively. The boiler has a nominal thermal heat input of 140 MJ/s.

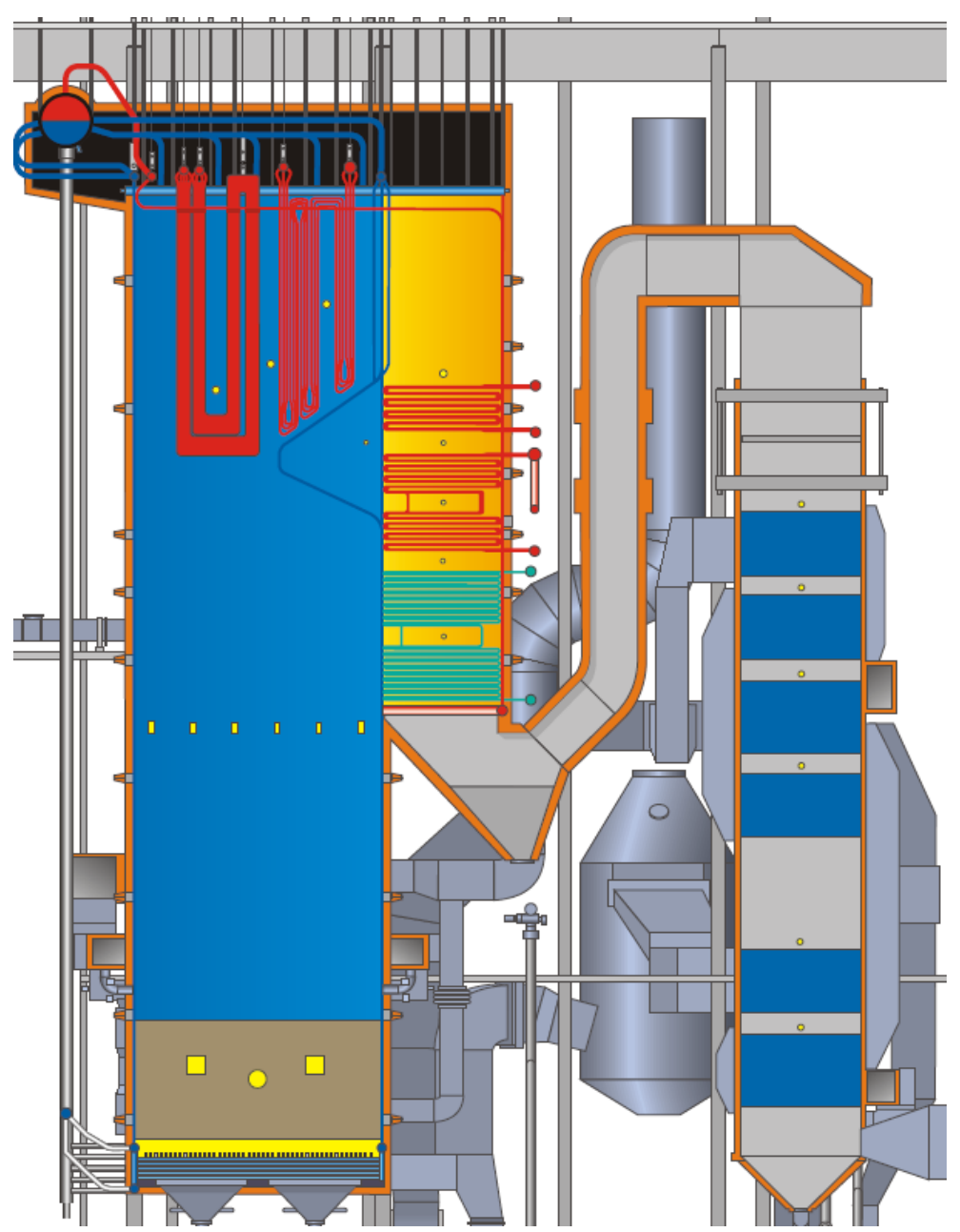


Figure 2: Schematic illustration of the ASV06 boiler.



3 Production of test material

3.1 SAMPLE RINGS

The sample rings used for the probe exposures were produced in different ways depending on alloy. In the upcoming sections, the manufacturing procedure will be briefly described.

3.1.1 Commercial alloys

The commercial alloy sample rings were made from tubes by cutting and machining to the desired dimensions. The tubes used for the 347H and 310HCbN sample rings were from the same batches as the ones that were inserted as fixed installations (see section 0). The Sanicro 25 sample rings were made from a tube that was produced and sent by Alleima.

3.1.2 Model alloys

The model alloy sample rings (Fe10Cr4Al, Fe10Cr4Al1Si and Fe10Cr3Al2Si) were produced by Kanthal. The melting was performed through induction heating in an argon containing low vacuum atmosphere. In the same protective atmosphere, the melt was cast in copper moulds into cylindrical ingots. To remove slag and segregations effects, the top of the ingots is cut off. The ingots are cut into three pieces and forged at 900 °C and pressed into the form of a puck (with the desired height). The pucks were finally made into rings through lathe machining.

3.1.3 Kanthal® EF101

The Kanthal® EF101 material was made through Kanthals full-scale production, which includes melting, purification of melt, casting and hot rolling. The hot rolled material was finally made into rings through lathe machining.

Sample rings coated with powder of Kanthal® EF101M (M for modified) were made with 347H as substrate. The 347H substrate ring was cut from 347H tubes and machined to the desired dimensions. EF101M was made into powder from the EF101 produced in the full-scale production described above. The material was first remelted and additional Si and Al was added so that the nominal composition was increased to 2 wt% Si and 5 wt% Al. The powder was produced through an atomization technique. The range of the powder particle size from the atomization was broad but the powder was sifted so that the particle size was ranging from 10-45 μm . The division of additive and subtractive manufacturing within the department of engineering sciences at University West utilized the high velocity air-fuel (HVAF) technique to coat the 347H sample rings with the EF101M powder. The nominal coating thickness was 400 μm .



3.2 FIXED INSTALLATIONS

Tubes of alloys 347H, 347HFG and 304HCu were produced to be welded onto the 310HCbN superheater tubes in a region of the tertiary superheater (in tube elements 23-25). The tubes were produced seamless and was cold-finished and solution annealed to achieve the finished tubes. Tube dimensional tolerances are according to material standards, e.g. EN 10216-5 and ASME SA-213. The nominal values of the tube dimensions are shown in Table 1.

Table 1: Grade and dimensions (nominal values) of fixed installed tubes and superheater tubes (310HCbNHCbN).

Material	Grade	Inner/outer diameter (mm)	Thickness (mm)
347H	X7CrNiNb18-10	24,5/38	6,3
347HFG	X8CrNi19-11	23,8/38	7,1
304HCu	KA-SUS304J1HTB	26,5/44,5	8,0
310HCbN	SA-213 TP310HCbN	27,9/38	4,5



4 Experimental procedure

4.1 LAB EXPOSURES

The corrosion behaviour of three different FeCrAl model alloys were investigated in a laboratory environment mimicking the environment (but simplified) of a biomass-fired boiler. The nominal chemical composition of the model alloys is given in Table 2.

 Table 2: Nominal chemical compositions of the FeCrAl model alloys used in this study.

Model alloys	Fe	Cr	Al	Si
FeCrAl 0Si	Bal.	10	4	0
FeCrAl 1Si	Bal.	10	4	1
FeCrAl 2Si	Bal.	10	4	2

4.1.1 Sample preparation

The samples were cut into coupons with a dimension of $10\times8\times2$ mm and a hole (1.5 mm in diameter) were drilled in the upper part of the coupons (for hanging the sample in the thermobalance). Prior to exposure, the sample coupons were ground with SiC paper from P500 to P4000 and were finally polished down to 1 μ m with diamond suspensions until a mirror-like surface was achieved.

4.1.2 Exposures

The samples were weighed using a Sartorius[™] balance with microgram resolution prior to exposure. After weighing, KCl was deposited on the surface of the samples by spraying a water-ethanol (20:80) solution saturated with KCl. A continuous flow of warm air was directed towards the sample during spraying to accelerate the drying of the solution. After spraying, the samples were weighed again to determine the amount of KCl deposited on the sample. The procedure was repeated until an amount of 1 mg/cm² was deposited on the samples.

Two types of lab exposures were performed in this study, using a horizontal silica tube furnace and a thermobalance. The tube furnace exposures were performed with a flow rate of 3 cm/s (calibrated by a Bios Definer 220M) and a gas composition of $5\%O_2 + 20\%H_2O + N_2$ (Bal.) at $600^{\circ}C$ for 168 hours. Reference exposures (in the absence of KCl) were also performed. Samples were mounted vertically in alumina sample holders in the same direction as the tube furnace. After the exposure the samples were weighed to measure the mass gain. The thermobalance exposures were performed using a Setaram Evolution TGA equipped with a Setaram Wetsys (to generate the desired humidity for the exposures). These exposures were performed in a similar environment but with a lower flow rate (about 1.5 cm/s) in the thermobalance. The samples were exposed for 48 hours. The samples were weighed before and after the thermobalance exposures to ensure that the correct mass gain had been recorded. Only one



sample could be exposed at a time in the thermobalance, and the exposures were therefore repeated at least three times to ensure reproducibility.

4.1.3 Analysis

Cross sections of the samples exposed for 168 hours in a tube furnace were prepared by attaching a thin Si wafer onto the sample surface using Loctite 415 glue. After the glue had dried for about 24 hours the samples were dry cut with a low-speed diamond saw and subsequently milled using a Leica TIC 3X broad ion beam (BIB) instrument to achieve a smooth surface for more detailed microstructural analysis. The three argon ion beam guns of the BIB instrument were operated at $8~\rm kV$ 6 hours.

The composition and morphology of the oxide scales were investigated by analyzing the cross sections of the exposed samples with scanning electron microscopy (SEM). An FEI Quanta 200 SEM equipped with an Oxford Instruments X-MaxN 80 T energy dispersive X-ray (EDX) detector was used for the SEM analysis in this work.

4.2 PROBE EXPOSURES

Three commercial grades (347H, 310HCbN, Sanicro 25) and one (347H) coated with an enhanced version (higher Al and Si content, 5.6-6-0 wt% and 2.4 wt% respectively) of the newly developed FeCrAl alloy Kanthal® EF101M), as well as four different FeCrAl model alloys (see Table 3), were exposed for 168h and 2000h (target exposure times) utilizing an air-cooled probe.

Table 3: Nominal composition of FeCrAl model alloys.

Model alloys	Fe	Cr	Al	Si
EF101	Bal.	12.4	3.7	1.3
EF101M	Bal.	12.4	5.0	2.0
Fe10Cr4Al 0Si	Bal.	10.0	4.0	0.0
Fe10Cr4Al 1Si	Bal.	10.0	4.0	1.0
Fe10Cr3Al 2Si	Bal.	10.0	3.0	2.0

4.2.1 Sample preparation

The materials used for the probe exposures were machined/cast and machined into rings (model alloys) with an inner diameter of 3.3 cm and a thickness of roughly 2 mm (as described in section 3). The EF101 coating on the 347H sample rings was produced by the thermal spraying technique, High Velocity Air-Fuel (HVAF). No further grinding/polishing was performed after the machining/thermal spraying. Prior to exposure, the exact thickness was measured at 8 points around each ring, using an Olympus 38DL PLUS Ultrasonic thickness gage.



4.2.2 Exposures

The probe exposures took place in two different boilers. The shorter exposure (target 168 hours) was performed in a commercial grate-fired Combined Heat and Power (CHP) boiler, the SKV402 boiler (boiler description found in section 2.1). The longer exposure (target 2000 hours) was performed in a commercial bubbling fluidized bed (BFB) CHP boiler, the ASV06 boiler (boiler description found in section 0). The short exposure was performed at two different superheater locations with different flue gas temperatures. Meanwhile, the longer exposure was performed at only one superheater location. In each location, sample rings were exposed to two different material temperatures, 600 °C and 700 °C. This was achieved using air-cooled probes (see Figure 3) incorporated with thermocouples and connected to a PID (Proportional-Integral-Derivate) controller which enables regulation of the material temperature by regulating the flow of pressurized air. The probe has two different temperature zones, enabling the exposure to two different material temperatures simultaneously with the same probe.

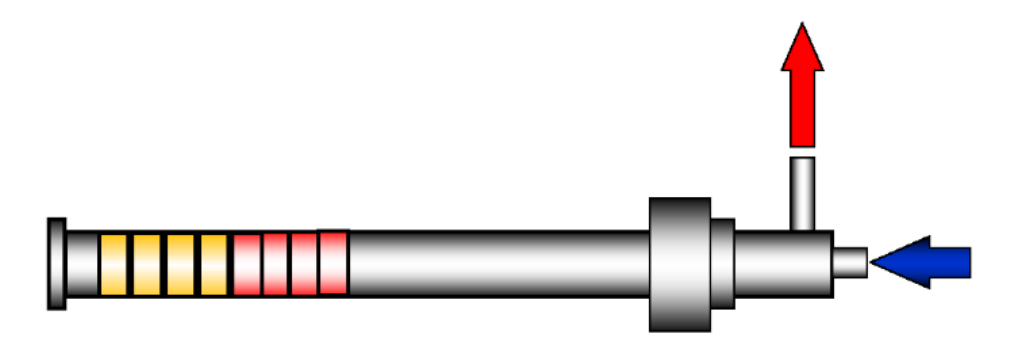


Figure 3: Schematic illustration of the air-cooled probes used for the probe-exposure. The red and yellow bands demonstrate the two heating zones (4 samples in each). The blue arrow represents the inlet of cool air while the red arrow represents the outlet of warm air.

Prior to exposure, deposit tests were performed at each location and material temperature to gage the corrosivity of the current boiler settings. For the longer exposure, a second and third deposit test was performed immediately after finishing the corrosion test and one week later, respectively. More detailed information regarding the experimental conditions in the two different boilers will be described in section 4.4. and in the appendix.

4.2.3 Analysis

The chemical composition (only anion concentration (Cl⁻ and SO₄²⁻) of the deposits was analyzed using ion chromatography (IC), using a Dionex ICS-90 system. The anions were analyzed with an IonPac AS4A-SC analytic column and 1.8mM NaHCO3/1.7mM NaHCO3 was used as solvent. The flow rate was 2ml/min. A representative and known amount of deposit was removed from the samples and dissolved in 100 mL distilled water. A 5 mL sample of this prepared solution was inserted into the IC column to obtain the amount of Cl ions and the S/Cl ratio.

Cross sections of the exposed sample rings were prepared by epoxy casting, followed by cutting, using a Stuers Secotom-10 precision cutting machine. The cross sections were polished (in absence of water to prevent interactions with



water soluble corrosion products) with SiC paper (P500 to P4000) and sputtered with a thin gold film to increase the conductivity (necessary for electron microscopy). The cross sections were analyzed by means of scanning electron microscopy (SEM) and energy dispersive X-ray (EDX) with an accelerating voltage of 20 kV using an FEI Quanta 200 equipped with an Oxford Instruments X-MaxN 80 T EDX detector. The thickness of the rings after exposure was measured at eight locations in similar positions as before exposure to evaluate the material loss.

4.3 FIXED INSTALLATIONS

Three tubes of different materials (347H, 347HFG and 304Cu) were welded onto the 310HCbN tubes in a location of the tertiary superheater (at tube elements 23-25).

4.3.1 Exposures

The tubes were installed before the boiler was put into operation in June 2019. The tubes were removed during the planned maintenance outage starting the 22nd of July 2022. Due to the low temperature during the early commission stage (because of low load), the number of hours the fixed installed tubes were exposed has been estimated to 22 000 hours (final estimation for total operation time is approximately 23 850 hours). The average material temperature of the fixed installed tubes has been estimated to 540 °C. This has been based on the average outlet steam temperature of tube element 25 (average steam temperature in the tube estimated to 532 °C and the approximation that the material temperature is approximately 10 °C higher). More detailed information on operating parameters during the period that the fixed installed samples were exposed in the boiler can be found in section 4.4 and in the appendix.

4.3.2 Analysis

The fixed installed tubes were cut into four sections (for each tube, see Figure 4) with the outer sections including the 310HCbN tube endings.

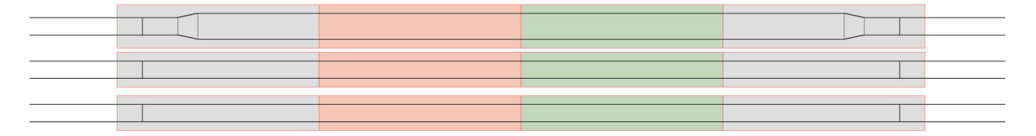


Figure 4: Schematic illustration of the sectioning of the removed fixed installed tubes (304HCu, 347HFG and 347H from upper to bottom). The outer segments (gray) contains both the welded test tubes and the 310HCbN-tube ending.

The tube sections were cut into smaller pieces before being cast in epoxy. The cast tube sections were cut to reveal the cross sections, which were prepared using mechanical grinding polishing to a surface finish of 6 μ m (P4000 SiC paper). Prior to SEM analysis, the polished cross sections were sputtered with a fine layer of gold to prevent charging of the epoxy during analysis. SEM analysis was performed using an FEI Quanta200 ESEM with an accelerating voltage of 20 kV.

Cross sections for light optical microscopy LOM were prepared by grinding to 4000-grit SiC paper and polishing using 3 μ m and 1 μ m diamond suspensions.



Samples were observed before etching and after etching in Kallings reagent (5g CuCl₂ in 100 ml hydrochloric acid) to reveal grain structures.

The material thickness (after exposure) and the thickness and composition of the corrosion products were analysed at 4 different points around the tube, including the leeward and windward sides. The material thickness after exposure was compared with the original tube thickness (obtained from measuring unexposed reference tubes) to gage the material loss.

4.4 EXPERIMENTAL CONDITIONS IN THE BOILERS

Details regarding exposures with air cooled deposit probes, air cooled corrosion probes and test tube sections in fixed installation will be given in the following sections.

4.4.1 Fuel

Both Skærbæk (SKV402) and Asnæs (ASV06) are wood chip-fired boilers mainly utilizing imported wood chips. Due to the fuel logistics practice from ship unloading to use in boilers, the reporting of wood chips characteristics will be average values based on a significant number of ship loads. Characteristics of imported wood chips are given as average values below.

A planned test with a fuel mix of wood chip and bark was initiated at Asnæs (ASV06) starting from 27.02.2022 and has therefore relevance for the Asnæs exposures with corrosion probe, deposit probe 2 and deposit probe 3. Details regarding operation will be given in the relevant sections. Characteristics of the bark used in these fuel mixes (reference: S.59105) are given below.

 Table 4: Characteristics of the bark used during the planned fuel mix test.

Parameter	Boiler	Imported wood chip average values	Bark (S.59105)
LHV	MJ/kg as received	10,3	4,14
Water	% as received	40,0	68,3
Ash	% dry	1,7	9,0
S	% dry	0,017	0,045
Cl	% dry	0,008	0,106
Al	% dry	0,05	0,58
Ca	% dry	0,58	0,87
Fe	% dry	0,03	0,40
K	% dry	0,12	0,33
Mg	% dry	0,04	0,14
Na	% dry	0,009	0,26
Р	% dry	0,020	0,040
Si	% dry	0,09	2,20



4.4.2 Fuel additives

Asnæs (ASV06) is designed with facilities for sulphur dosing to the fuel according to Valmet design. Sulphur dosing is limited to periods with high steam temperatures and is added to the fuel as sulphur granules on conveyer belt before buffer silos.

Evaluation of sulphur dosing during the complete operation period indicate a typical range of 0.2 - 0.8 kg sulphur / ton dry biomass when sulphur dosing has been activated. Average sulphur dosing, when activated, has been estimated at approximately 0.44 kg sulphur / ton dry biomass.

4.4.3 Skærbæk (SKV402)

As mentioned in section 4.2.2, the exposures at SKV402 included a set of air-cooled deposit probes and a set of short-term air-cooled corrosion probes (600 °C and 700 °C for both deposit and corrosion tests).

Deposit test

The air-cooled deposit probes were inserted in the boiler the 12th of December 2019 and remained there for three hours (between 12:00 and 15:00). During this period, the boiler was under normal operation with wood chips (characteristics according to average values for imported wood chips). The boiler was run at 95-100% load during 90% of the total exposure time and at 90-95% load during the remaining exposure time.

The deposit probes were inserted in two positions, through openings in modified inspection doors. Both were installed at boiler left side wall in the superheater area. Reference to position A and position B can be made according to Figure 5. Position A and B refers to the positions with a higher/lower flue gas temperature respectively.



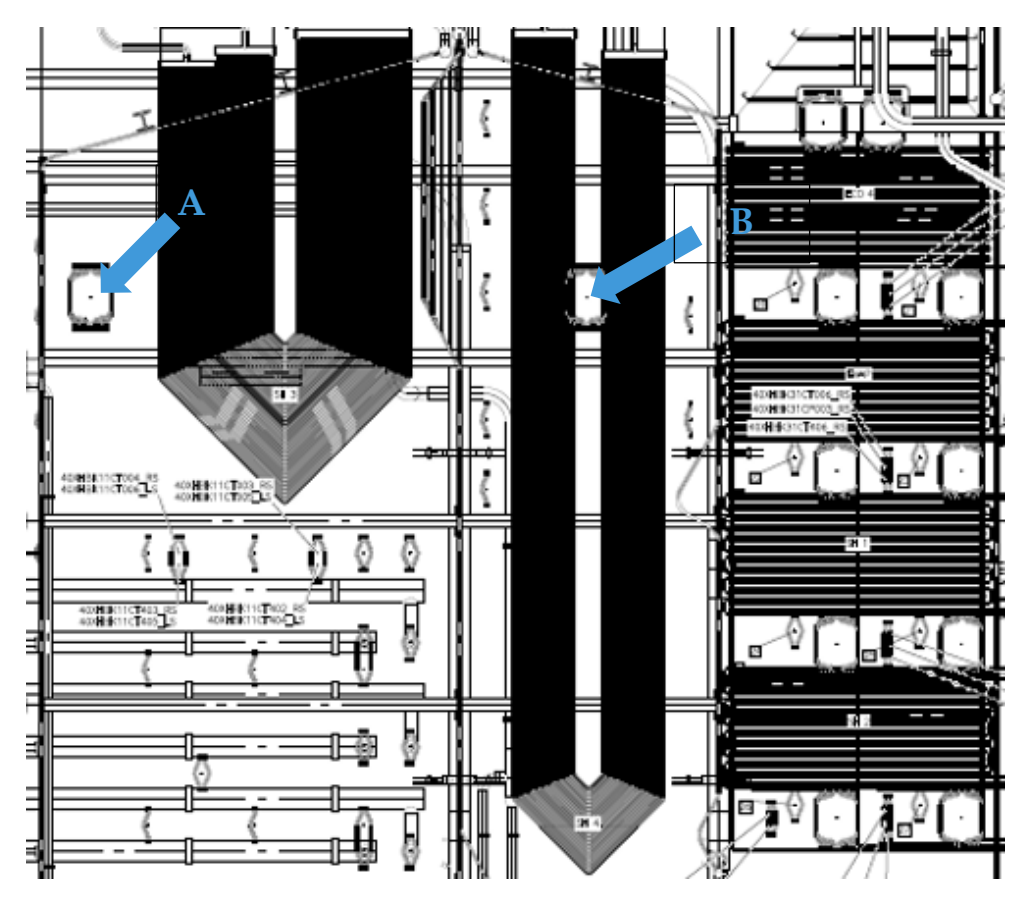


Figure 5: Schematic illustration of SKV402, showing the positions of the modified inspection doors.

Flue gas temperatures are reported for three selected positions: before superheaters, first pass top and second pass top (see Appendix). Exposure position A is considered best represented by flue gas temperature before superheaters and exposure position B is considered best represented by flue gas temperature at second pass top. The flue gas temperature before the superheaters was relatively stable during deposit test, ranging from 920 °C to 960 °C. The flue gas temperature at the top of the second pass was also relatively stable, ranging from 740 °C to 780 °C.

Corrosion test

The air-cooled probes for the corrosion test were inserted in the two positions 20:00 the 12^{th} of December 2019 and was removed 10:00 the 20^{th} of December 2019, resulting in a total exposure time of 182 hours. The boiler was under normal operation with wood chips (characteristics according to average values for imported wood chips) during the period of the exposure. The boiler load was varying between 50% and 100% (only considering parameters that remained during $\geq 5\%$ of the total exposure time) during the corrosion test. The flue gas temperature before the superheaters was ranging from 840 °C to 980 °C while the flue gas temperature at the top of the second pass was ranging from 600 °C to 720 °C. More details are found in the Appendix.



4.4.4 Asnæs (ASV06)

As mentioned in sections 4.2.2 and 4.3.2, the exposures at Skærbæk (SKV402) included three exposures with air-cooled deposit probes and exposure with one set of medium term (between the first and second deposit test) air-cooled corrosion probes as well as a set of test tube sections in the fixed installation in tertiary superheater.

Deposit tests

All deposit tests were performed at two material temperatures ($600 \, ^{\circ}\text{C}$ and $700 \, ^{\circ}\text{C}$), achieved with the air-cooled probes. The corrosion probes were inserted into service deck openings in the positions marked A and B in Figure 6. Position A was used for the deposit/corrosion probes with a material temperature of $700 \, ^{\circ}\text{C}$ while position B was used for the deposit/corrosion probes with a material temperature of $600 \, ^{\circ}\text{C}$.

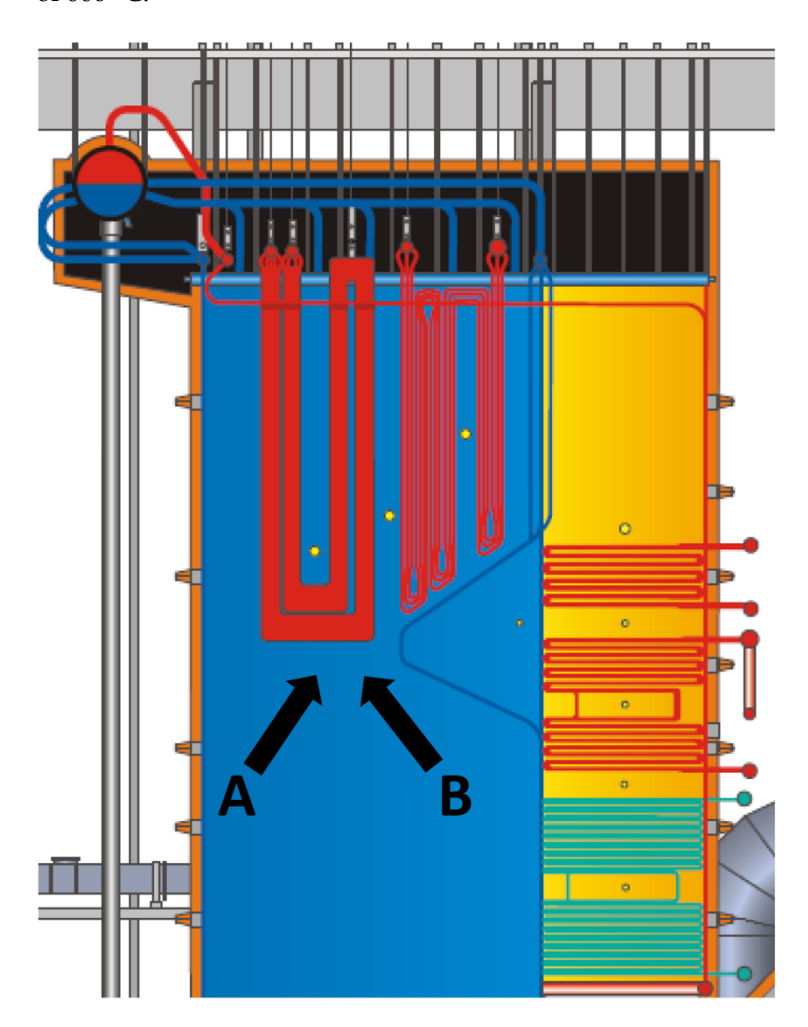


Figure 6: Schematic illustration of ASV06, showing the positions of the service deck openings.

The first deposit probe was installed 12.15 on the 7th of December 2021 and was removed 8.30 the 8th of December 2021, resulting in a total exposure time of 20 hours. During this period, the boiler was under normal operation with wood chips as fuel (characteristics as average values for imported wood chips). Additionally,



sulphur granules were added as a corrosion additive according to standard operation procedure. Operational data indicates that sulphur dosing was active during approximately 73% of the exposure period. The boiler load was varying between 35% and 85% but was in the range 75-85% during the majority of the exposure. The temperature at the exposure positions is best represented by the furnace temperature which was in the range 600-800 °C. More details can be found in the Appendix.

The second deposit probe was installed 12.10 the 1st of March 2022 and removed 09.00 the 2nd of March 2022, resulting in a total exposure time of 21 hours. During this period the boiler was under test operation with wood chips and 22 wt% bark (fuel characteristics according to Table 4). Additionally, no sulphur dosing was used during this test operation. Boiler load was ranging between 30% and 90% but during the majority of the exposure the boiler load was in the ranges 30-45% and 80-90%. The furnace temperature was ranging from 560 °C to 800 °C but during the majority of the exposure the furnace temperature was in the ranges 580-640 °C and 740-800 °C. More details can be found in the Appendix.

The third deposit probe was installed 10.45 the 9^{th} of March 2022 and removed 11.15 the 10^{th} of March 2022, resulting in a total exposure time of 24,5 hours. During this period the boiler was under test operation with wood chips and 22 wt% bark (fuel characteristics according to Table 4). Unlike the second deposit test, sulphur dosing was used during third deposit test. The boiler load was ranging largely between 25% and 90% but more frequently around 30%, 60% and 80%. The furnace temperature was ranging from 560 °C to 800 °C but more frequently around 580 °C, 670 °C and 760 °C. More details can be found in the Appendix.

Corrosion tests

The corrosion probe was installed 09.00 the 8^{th} of December 2021 and was removed 10.00 the 1^{st} of March 2022 resulting in a total exposure time of 1993 hours. The boiler was under standard operation with wood chips during most of the exposure period. Sulphur granules were added as a corrosion additive according to standard operation procedure. Operational data indicates that sulphur dosing was active during approximately 66% of the exposure period. Forced changes in the fuel mix and corrosion additive occurred during the last few days of the corrosion test. During those days the test conditions were similar to those specified for the second deposit test. The boiler load was ranging largely between 25% and 90% but more frequently around 40% and 80%. The furnace temperature was ranging from 560 °C to 820 °C but more frequently around 600 °C and 760 °C. More details can be found in the Appendix.

The test tube sections (fixed installations) were installed from fabrication and commissioning of the boiler in 2019 and was removed during the planned maintenance outage starting the 22nd of July 2022. The total operation time for the test tube sections was approximately 23 850 hours (based on recorded first fire in June 2019). Operation data related to the test tube sections have been analyzed for the period from 22.10.2019 00:00 to 23.07.2022 23:59. Analysis is based on operation data from 10 minutes interval query for the complete analysis period. Analysis period is 24.144 hours. Operation time with data confirming load, pressure and



temperature in the analysis period has been estimated to 22.125 hours. Further analysis of the commissioning and initial operation period with DCS data (from first fire to start of analysis period) have demonstrated additional 1.725 hours should be added. These data lead to the final estimate for total operation time at approximately 23.850 hours.

It should be noted that evaluation of operation data for reporting of load and temperature distributions has been based on the analysis period excluding commissioning and initial operation period. Reported distributions are considered representative for the total operation time.

Test tube sections in the fixed installation were installed in tertiary superheater trailing tubes at superheater outlet. Test tube sections were installed in superheater banks (elements) 23 - 24 - 25, see Figure 7.

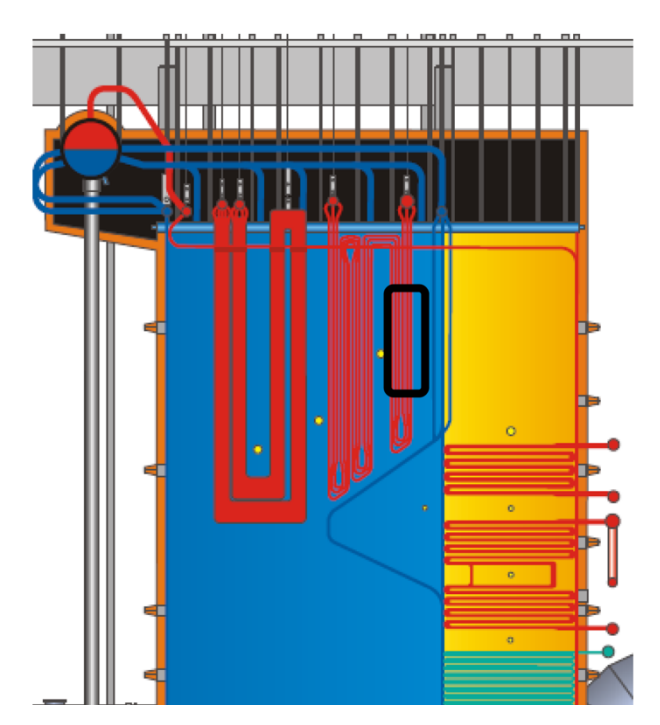


Figure 7: Schematic illustration of ASV06, showing the position of the fixed installed tube sections (black rectangle).

The boiler was run under standard operation with wood chips during most of the operation period. Sulphur granules were added as a corrosion additive according to standard operation procedure. Operational data indicates that sulphur dosing was active during approximately 50% of the operation period. As previously mentioned, limited test periods with forced changes of fuel mix and corrosion additive overlapped the operation with fixed installation. These short test periods may however be considered to have a negligible effect with reference to the high total operation time.

The flue gas temperature after the tertiary superheater is considered to best represent the flue gas temperature at the position of the test tubes. The recorded flue gas temperature was varying between 440 °C and 600 °C. The steam



temperature of tube element 25 of the tertiary superheater (considered to be representative of the temperature of the steam through the test tube sections) varied between 475 °C and 575 °C with an average of 532 °C during the entire operation time. Considering the limited convective heat flux in this area a reasonable assumption is that the material temperature of the test tube sections is 10 °C above the steam temperatures for tube element 25, i.e. averaged to approximately 540 °C. More details are found in the Appendix.



5 Oxidation simulation

Environmental degradation due to high-temperature corrosion is controlled by the properties of the oxide scales that form on the material. Iron-based alloys are generally used in high-temperature applications, i.e. low-alloy steels, stainless steels and FeCrAl alloys. Despite the large variety of the alloy grades, the protective layer formed in these alloys can be categorized into three major types of oxides: iron oxide (steels), Cr-rich oxide of M2O3 (stainless steels) and Al-rich M2O3 (FeCrAl alloys). The naturally grown oxides in these alloys may be defined as the alloy systems primary protection, while the secondary protection is defined as the oxide scales formed after breakaway oxidation [3].

The Calphad approach has been successfully applied in quantitative diffusion process simulations for a number of industrially important material systems, such as steels and superalloys, as well as with coatings. Diffusion modelling in oxides is more challenging and has been under development during the recent years, and the first models for iron, chromium and aluminum oxides are now available [6]. These models were used in this project together with characterization techniques (SEM) in order to predict oxide growth rates on probe samples exposed in boilers as well as on fixed installed material in a boiler.

Previous investigations have shown that different alloy grades form different protective scales at different stages, i.e. the primary and secondary corrosion regimes [3]. In the case of stainless steels, FeCr(Ni,Al) alloys, Cr-rich oxide forms at $600\,^{\circ}$ C, these alloys are thus called chromia forming alloys. In FeCrAl alloys with an Al concentration higher than 3 wt%, α -alumina can form. These alloys are categorized as alumina forming alloys. The formation of α -alumina is very slow at lower temperatures (around $600\,^{\circ}$ C) at which transient forms of alumina (lower corrosion resistance than α -alumina) forms. Thus, to achieve the formation of α -alumina, FeCrAl alloys generally need to be exposed at higher temperatures, i.e. $900\,^{\circ}$ C. In almost all cases, if breakaway oxidation occurs (transition into the secondary corrosion regime) for these material classes (steel, stainless steel, FeCrAl alloys), iron oxide forms at all temperatures.

These findings have been used in our previous work to develop lifetime prediction models for different material classes [6]. It has been shown that Cr and Al oxidation simulations can be a reliable representative for lifetime prediction in the chromia-alumina forming alloys within the primary corrosion regime while iron oxidation simulations may accurately predict the lifetime of the oxide after breakaway (secondary protection).

The simulation results for the oxide thickness (for chromia, alumina and iron oxide) after 168, 2000 and 22 000 hours can be compared with the experimental results from the probe exposures and fixed installations. For chromia and iron oxide the material temperature at for the calculations were 600 and 700 °C in accordance with the experimental values. Calculations for temperatures below 600 °C (to be compared with fixed installations) have not been performed due to insufficient diffusion data in the databases (below 600 °C) used for iron oxidation. For the alumina, the temperature input was set to 900 °C due to insufficient



diffusion data for alumina at 600 and 700 °C. The inputs, such as oxide type and grain size will be obtained from the microscopy investigation and previous laboratory work respectively.

Thermo-Calc Software AB is acknowledged for their support (Andersson J.O., Helander T., Höglund L., Shi P.F., and Sundman B., (2002). Thermo-Calc and DICTRA, Computational tools for materials science. *Calphad*, 26, 273-312.).



6 Results and Discussion

In order to achieve the overall goal of the project two parallel approaches has been taken. The first approach has been to investigate the performance of new materials, such as FeCrAl alloys, and compare these to the type of materials that are current in use in biomass-fired boilers. This has been done by means of carefully planned laboratory exposures, probe exposures within two different biomass-fired boilers and by investigating sample tubes installed in the tertiary superheater. The second approach has been to generate new knowledge regarding corrosion simulations and investigate the possibility to provide predictions of the corrosion rates in laboratory - probe - fixed installed materials. These approaches have been implemented in parallel on the same samples but will be reported separately in the following sections.

6.1 LAB EXPOSURES

The corrosion resistance of FeCrAl alloys have been studied extensively at high temperatures (900-1300°C) at which they are known to form a protective α -alumina scale, attributing to their excellent corrosion resistance [7-9]. Because of the protective α -alumina scale in this temperature range, FeCrAl alloys are commonly used as heating elements for various applications, for example the electrical elements of gas burners, furnace rollers and ignitors.

Below 900 °C, the formation of α -alumina is slower and less protective transient allotropes of alumina instead forms in the initial stages of the oxidation process. Previous studies have shown that FeCrAl alloys may form a thin transient alumina scale at 600 °C [10] which contains significant amounts of both Fe and Cr [11], making them more sensitive towards water vapor and the alkali-containing compounds found in biomass-fired boilers since it reacts with these species through two different reactions: Cr evaporation due to volatilization of chromium-oxy-hydroxide in the presence of water vapor [12]; and the formation of alkali chromates during reaction with alkali salts [13-17]. The loss of the chromia/alumina scale, which can be considered the primary protection of the alloy [3], is usually followed by the formation of fast-growing Fe-rich oxide, resulting in rapid material degradation and high maintenance costs.

Minor additions of Si have been shown to significantly improve the corrosion resistance of stainless steels [18-29]. The FeCrAl model alloys presented in the present study displays this positive effect when exposed in the presence of water vapor at 600 °C, see Figure 8. Figure 8a) and d) shows that FeCrAl0Si has formed a thick iron-rich oxide scale while b) and c) shows that both FeCrAl1Si and FeCrAl2Si has retained the primary protection, i.e. the initial chromia/alumina scale. This indicates that the primary protection becomes less sensitive towards the presence of water vapor upon the addition of Si, and thereby preventing breakaway oxidation. More details can be found in [20]. Asokan et al. showed that the primary oxide scale of the FeCrAl model alloys became more Al-rich upon the addition of Si which may explain the reduced sensitivity towards water vapor.



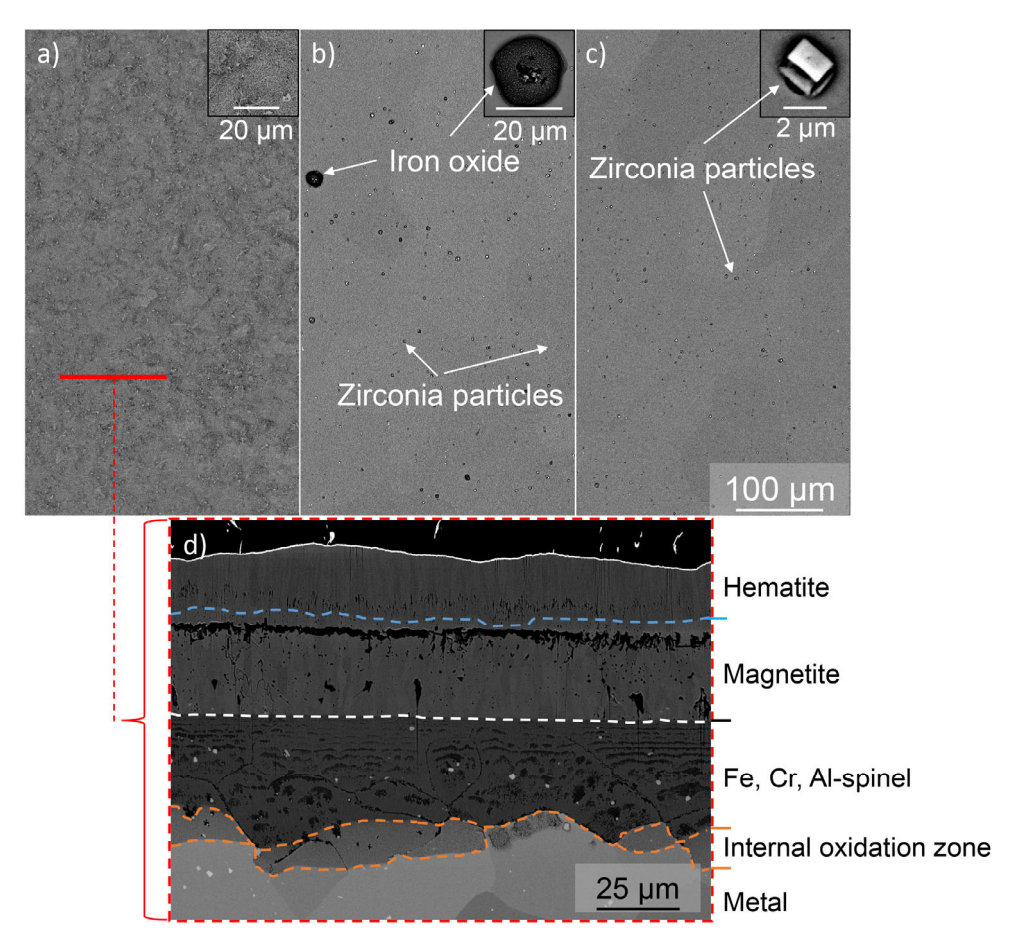


Figure 8: SEM-BSE plan view images of a) FeCrAl0Si, b) FeCrAl1Si and c) FeCrAl2Si after exposure to $O_2+H_2O+N_2$ at 600 °C for 168 hours. The cross section of FeCrAl0Si is shown in d).

The commercial stainless steels 304L (composition similar to 347H) and 310HCbN has been shown to behave slightly different to the FeCrAl alloys. In the presence of water vapor, these stainless steels have been shown to partially experience breakaway oxidation while other areas remain protective [12, 30-33]. While this is a significantly better situation than what is observed for the FeCrAl0Si alloys (which forms a fast-growing iron-rich oxide covering the entire surface), the minor additions of Si to the FeCrAl alloys prevents the formation of iron oxide islands. The Si-containing FeCrAl alloys therefore displays a corrosion resistance superior to that of the stainless steels under humid conditions.

In the presence of alkali chlorides, alloys tend to lose the primary protection regardless of how highly alloyed they are, thereby forcing the alloys into the secondary corrosion regime (forming fast-growing iron-rich oxide). However, minor additions of Si have been shown to reduce the corrosion rate significantly even after this transition occurs [16, 34, 35]. Accordingly, when exposing the alloys presented in this study in the presence of water vapor and KCl, the oxidation rate was shown to be significantly reduced upon the addition of Si, see Figure 9.



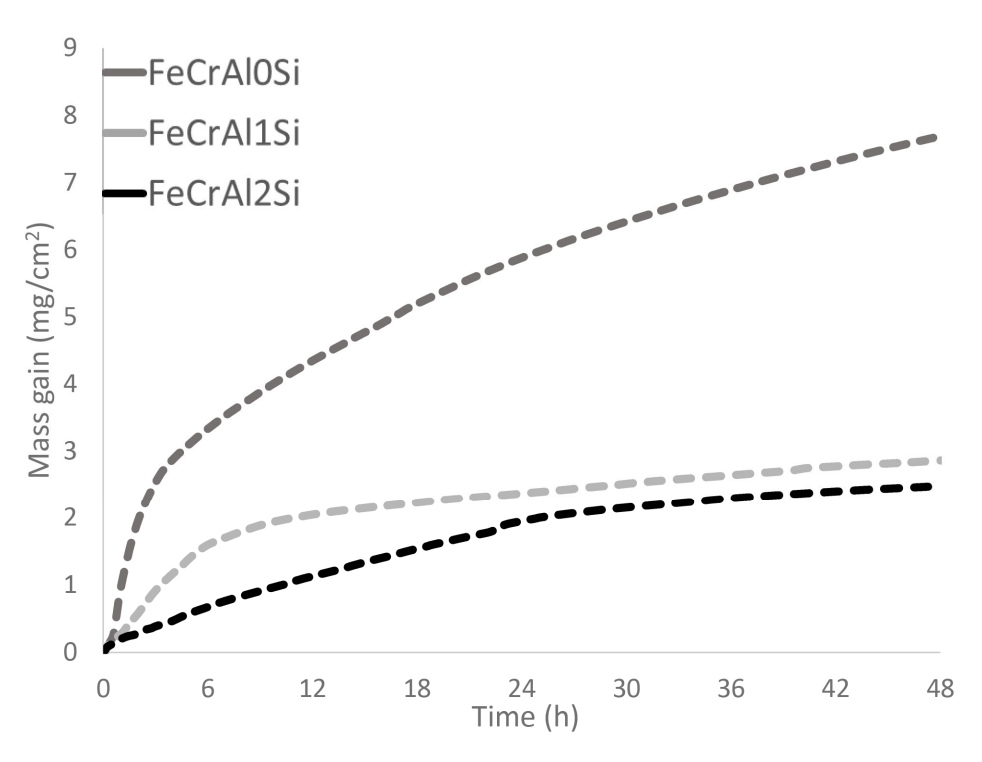


Figure 9: Graph showing the mass gain of the three FeCrAl model alloys after exposure to $O_2+H_2O+N_2$ in the presence of KCl at 600 °C for 48 hours in a thermobalance.

The microstructure of the oxide scales, formed after 168 hours of exposure, is shown in Figure 10 and Figure 11. They show that all three alloys have formed an iron-rich oxide scale and has therefore transitioned into the secondary corrosion regime. The main difference in oxide microstructure, apart from the oxide thickness, between FeCrAl0Si and the Si-containing alloys is the absence of an internal oxidation zone underneath the oxide scale for the latter.

The internal oxidation zone has been proposed to be a key component, responsible for the rapid oxidation observed for alloys with a poor secondary protection [36-38]. The internal oxidation zone, which consists of Cr-rich spinel precipitates surrounded by an Cr-depleted (Fe-rich) alloy matrix, rapidly oxidize as the corrosion front approaches and is suggested to result in rapid Fe-leaching and the formation of a poorly protective porous oxide scale for which the kinetics are limited by iron oxidation [39]. Additionally, preventing the internal oxidation has been shown to facilitate the formation of a healing layer which further reduces the oxide growth rate.



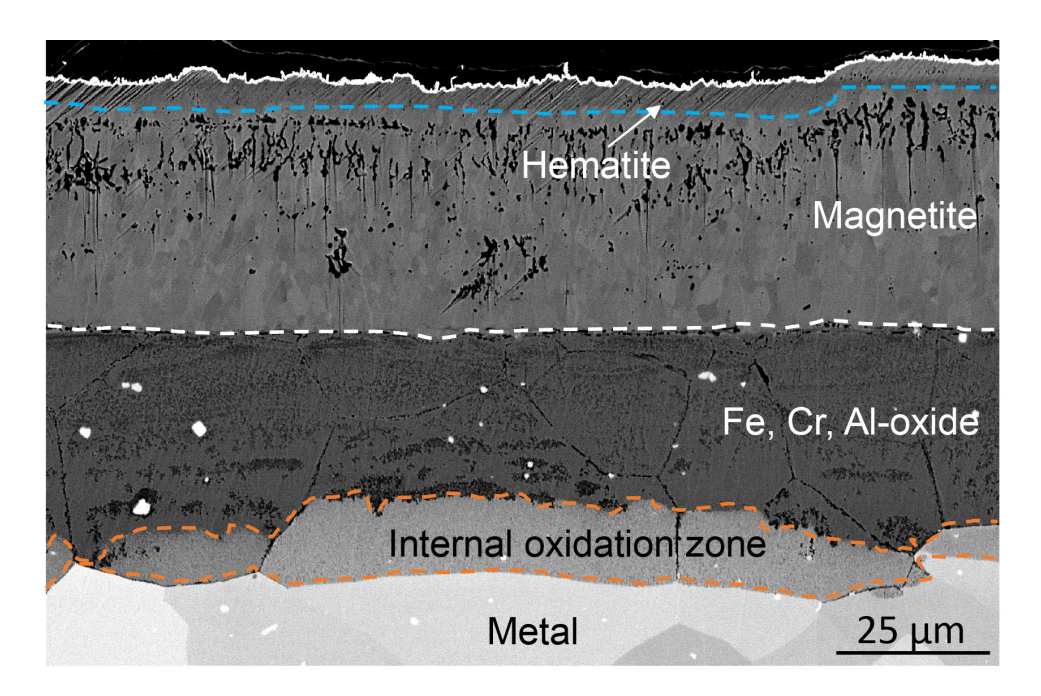


Figure 10: SEM-BSE cross section image FeCrAlOSi after exposure to $O_2+H_2O+N_2$ in the presence of KCl at 600 °C for 168 hours.

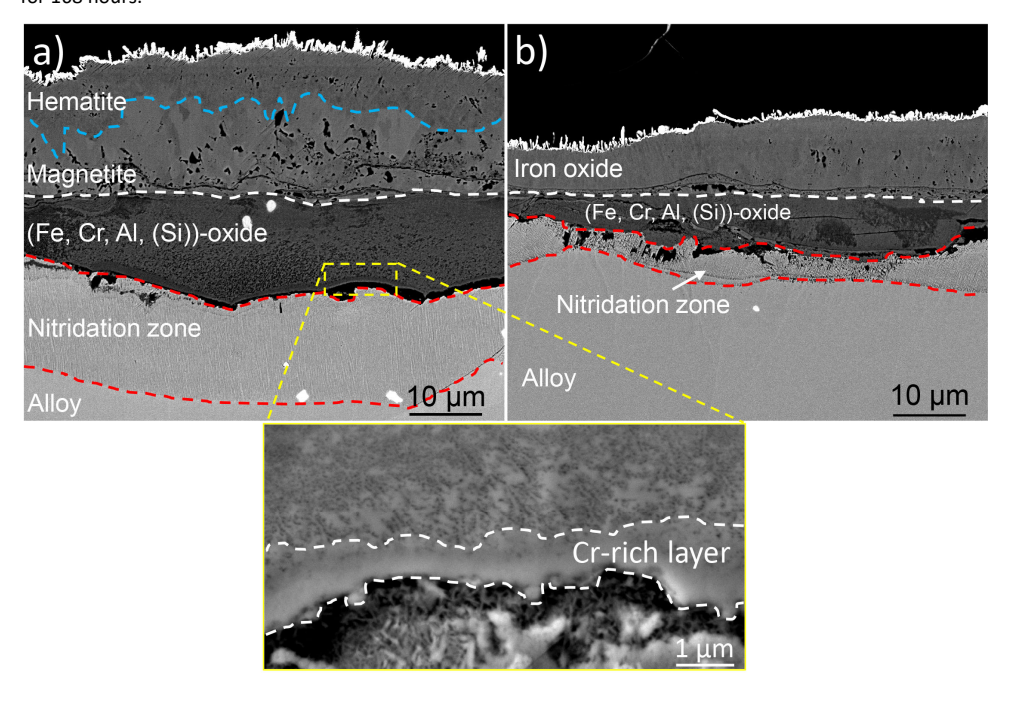


Figure 11: SEM-BSE cross section image a) FeCrAl1Si and b) FeCrAl2Si after exposure to $O_2+H_2O+N_2$ in the presence of KCl at 600 °C for 168 hours.

Thermodynamic equilibrium calculations showed that Al and Cr affects the stability of the internal oxidation zone, see Figure 12. The phase diagrams shows that Al reduces the stability range of the internal oxidation zone, thereby reducing the Cr concentration necessary to inhibit internal oxidation. Eklund et al. [38] suggested that Si has an additional effect on the stability of the internal oxidation zone by indirectly increasing the Cr and Al concentration by occupying the tetrahedral sites (originally occupied by Fe²⁺ ions), creating vacancies on the tetrahedral sites (to maintain charge neutrality because of the higher valency of the



Si⁴⁺ ions) and thereby reducing the total amount of ions in the spinel crystal structure. Since the Cr and Al ions occupy the octahedral sites, the total number of these alloys will not be affected and therefore the concentration of these will increase. This hypothesis is further explained in the published article [38].

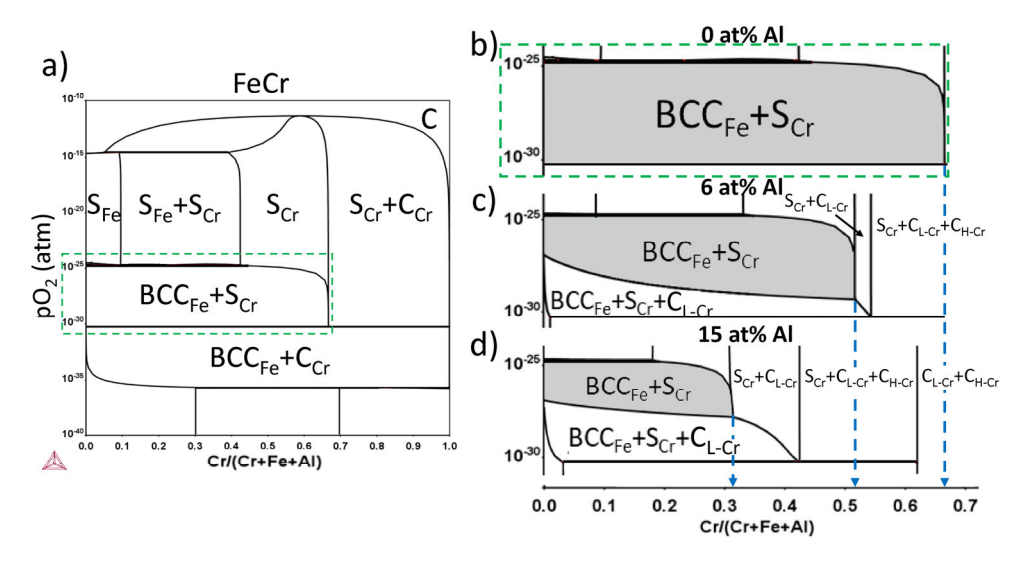


Figure 12: Phase diagrams of the Fe-Cr-Al-O system showing the effect of Cr and Al on the stability of the internal oxidation zone ($BCC_{Fe}+S_{Cr}$).

Commercial austenitic stainless steels, such as 304L, generally displays a better performance after breakaway oxidation in this type of environment (presence of alkali chlorides). Ferritic stainless steels often form fast-growing iron-rich oxide, similar to FeCrAl0Si while the austenitic stainless steel tend to form an inward-growing scale that is highly enriched in Cr, facilitating the formation of a corundum-type healing layer [13, 40, 41]. This effect was also observed by Persdotter et al. [3] for Ferritic Ni-containing alloys, indicating that this may be a Ni-effect. However, the FeCrAl2Si displays a corrosion rate that is in the same range as 304L and other similar austenitic stainless steels [40]. Eklund et al. showed that the corrosion rate could be further reduced by increasing the Cr content in Sicontaining FeCrAl alloys [38]. The Fe20CrAl2Si, with a Cr content similar 304L, formed a 3-4 μ m thick oxide scale after 24 hours of exposure in a humid KCl-rich environment at 600 °C. This can be compared to the roughly 20 μ m thick oxide scale formed on the surface of 304L when exposed in the same environment [40].

In summary, minor additions of Si have been shown to improve both the primary and secondary protection of FeCrAl alloys which is promising when it comes utilize these types of materials in harsh environments below their optimal temperature range.

6.2 PROBE EXPOSURES

All samples from the short-term (target 168 hours) and long-term (target 2000 hours) exposures were analyzed with SEM to investigate both material loss and type of corrosion product/deposit formed on the surface of the sample rings. The thickness measurements showed that the material loss was lower than the error



margin of the pre-exposure measurements and was close to zero for all samples after both the short-term exposure and the long-term exposure. This indicates that both boilers exhibit very mild environments during the time-period of the corrosion tests.

The ion chromatography (IC) measurements from the short-term exposure showed no clear trends between the different positions and material temperatures. The Cl-concentration in the deposit varied between 0.05 and 1.25 wt% while the SO₄²⁻ concentration varied between 1 and 13 wt%. This results in a S/Cl ratio that varies between 3 and 125. Previous studies have shown that corrosion rates increase significantly below a S/Cl ratio of 2 while exceeding this value reduces the corrosivity of the boiler environment [42-44]. This means that the chemistry of the deposit formed during the short-term exposure was very mild, which is in agreement with the very low material loss.

The IC measurements from the long-term exposure did not show any effect of the material temperature on the chemical composition of the deposit. As described in section 4.2.2, deposit was collected both before and after the long-term exposure. Prior to exposure, the Cl- concentration was around 0.02 wt% while the concentration of SO₄²- was around 40 wt% which results in a S/Cl ratio of 2000. Immediately after the exposure, the collected deposit contained 0.02-0.1 wt% Cland 12-20 wt% SO₄²⁻ which results in a S/Cl ratio of 120-1000. As explained in section 4.4.4, a test operation with 22 wt% bark in addition to the wood chips was performed (without sulphur dosing) during this deposit test. This strongly indicates that the deposit chemistry during the long-term exposure was even milder than for the short-term exposure. The third deposit test (one week after the second) displayed a Cl⁻ concentration of 0.8-0.9 wt% and SO₄²⁻ concentration of 27-30 wt% which results in a S/Cl ratio of 30-38. This is a lower S/Cl ratio than what was obtained from the deposit test in the SKV402 boiler which means that exposure under these conditions (described in section 4.4.4) may result in a higher corrosivity than what was observed in SKV402.

The corrosion product data for the short-term and long-term tests, obtained from the SEM analysis, is summarized in Table 5 and Table 6, respectively. The data has been translated into the extent of breakaway oxidation, i.e. how much of the sample ring that remains in the primary corrosion regime (chromia/alumina), or have transitioned into the secondary corrosion regime (iron-rich oxide), for each sample and condition. Examples of these types of corrosion stages are shown in Figure 13 and Figure 14.



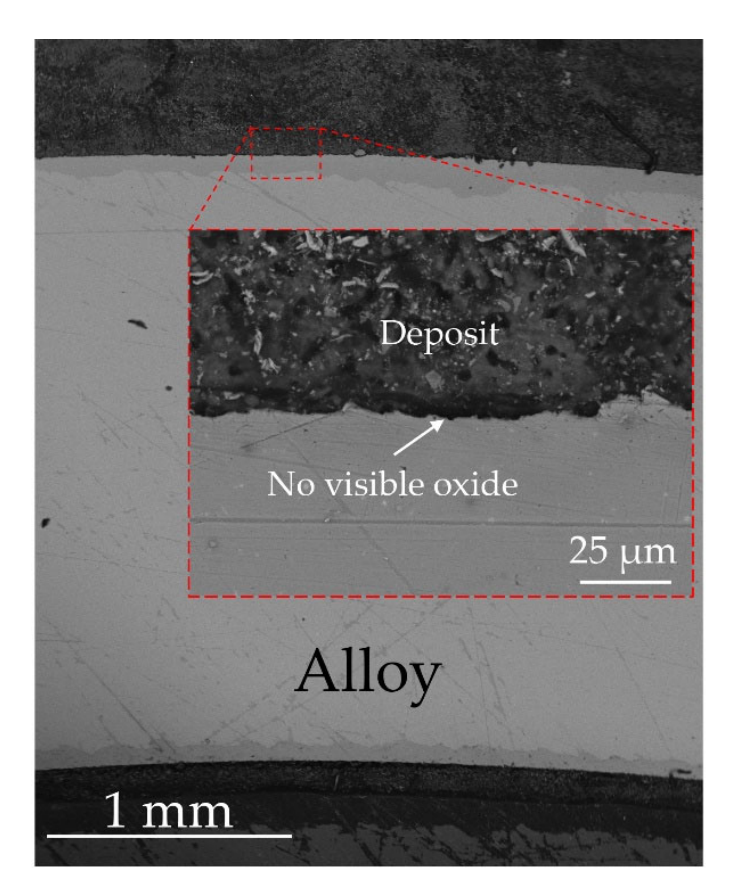


Figure 13: SEM-BSE image of the Fe10Cr3Al2Si alloy after long-term probe exposure at a material temperature of 600 °C. This image serves as an example of an area that has retained the primary protection (resisted breakaway oxidation)



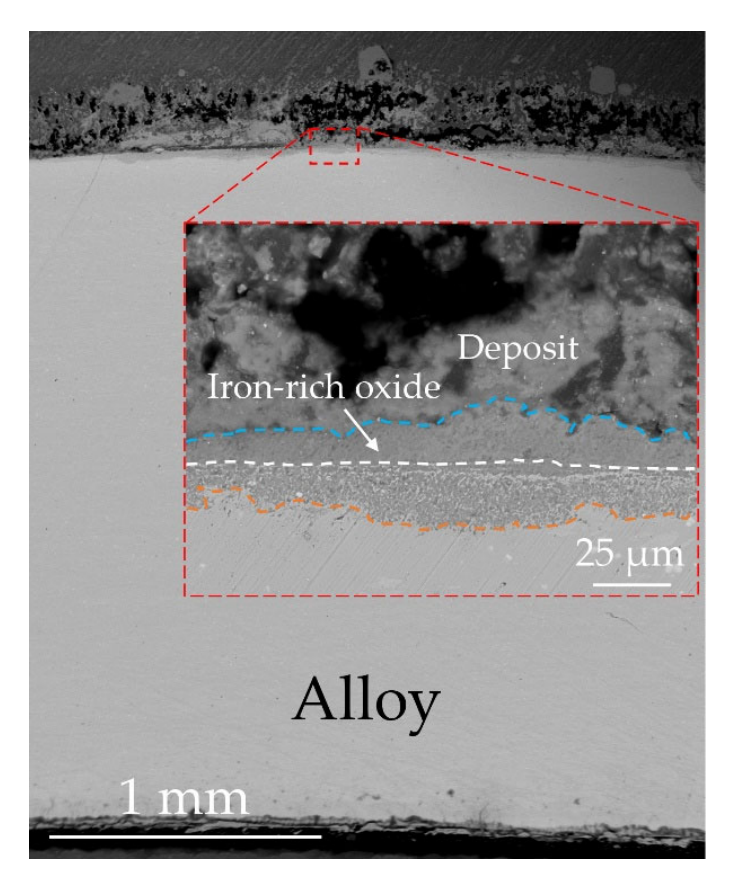


Figure 14: SEM-BSE image of alloy 310HCbN after short-term probe exposure at high flue gas temperature and a material temperature of 600 °C. This image serves as an example of an area that has transitioned into the secondary corrosion regime.

While the material loss is low for all investigated alloys, the data from the short-term exposure (Table 5) shows a clear difference in corrosion resistance between the stainless steels and the FeCrAl alloys. A relatively large fraction of the stainless steels transitioned into the secondary corrosion regime and has formed fast-growing iron-rich oxide. Among the stainless steels, 347H and 310HCbN seems to be performing better than Sanicro 25, for which a larger portion of the alloy surface has experienced breakaway oxidation in most of the investigated conditions. No clear trend can be observed for the stainless steels in relation to the different superheater positions (low and high flue gas temperature), but the data indicates that the extent of the corrosion attack is higher at 600°C than at 700°C.



Table 5: Summary of data obtained from SEM analysis of all probe-samples after exposure for 168 hours in the Skærbæk boiler.

-				
Alloy	Low flue gas	temperature	High flue gas	temperature
Alloy	600C	700C	600C	700C
		Majority	Majority	Majority
347H	Secondary	Primary	Secondary	Primary
	Majority	Majority		Majority
310HCbN	Secondary	Primary	50/50	Secondary
		Majority		
Sanicro 25	Secondary	Secondary	Secondary	50/50
		Majority	Majority	
EF101	50/50	Primary	Primary	Primary
Fe10Cr4Al0Si	50/50	Primary	Primary	Primary
			Majority	
Fe10Cr4Al1Si	Primary	Primary	Primary	Primary
	Majority			
Fe10Cr3Al2Si	Primary	Primary	Primary	Primary
347H with				
EF101	Primary	Primary	Primary	Primary

The effect of temperature is further demonstrated in Figure 15, which shows representative areas of the Sanicro 25 and Fe10Cr4Al0Si sample rings. While the IC measurements did not display any significant differences in deposit chemistry when changing the material temperature, the SEM analysis indicates an increased presence of Cl-containing species (such as KCl) in the deposit after being exposed to a material temperature of 600 °C. Consequently, the sample rings display breakaway oxidation to a larger degree at this temperature. A higher deposition rate of KCl at a material temperature of 600 °C than at 700 °C should be expected, especially if the flue gas temperature is significantly higher than the lower material temperature. The equilibrium vapor pressure of potassium chloride (KCl) is dependent on and increases with temperature [45]. Thus, if high-temperature flue gas that has reached the saturation pressure of KCl(g) comes into contact with a cooler surface, the temperature decrease of the flue gas will reduce the equilibrium vapor pressure of KCl(g) which will force the gas to deposit the excess KCl in solid form onto the cooler surface. This concept was utilized by Phother et al. to continuously deposit KCl(s) on metallic samples in a laboratory environment mimicking the biomass-fired boiler environment [46].



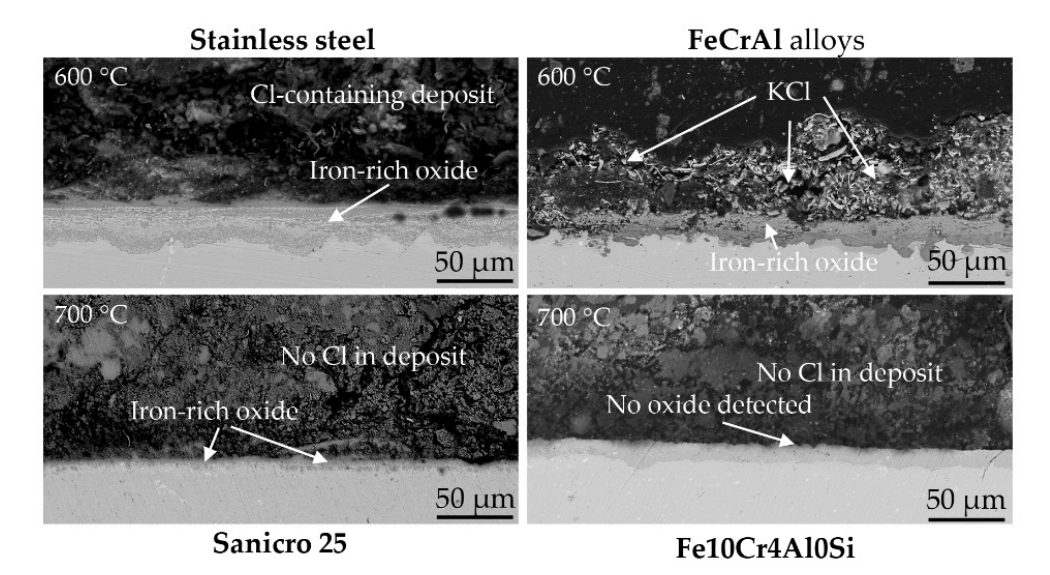


Figure 15: SEM-BSE images of representative areas of the sample rings of Sanicro 25 and the Fe10Cr4Al0Si alloy after the short-term exposures at 600 °C and 700 °C.

In addition to the temperature effect on the deposit chemistry, Figure 15 also demonstrates that the FeCrAl alloys were better at resisting breakaway oxidation in the absence of Cl-containing deposit compared to the stainless steels while both material classes behaved similar in the presence of Cl-containing deposit (displayed breakaway oxidation). However, Figure 16 shows that the more highly alloyed EF101 is even able to resist the presence of KCl (in about 50% of the cases) compared to the relatively lean Fe10Cr4Al0Si alloy which displays breakaway oxidation in all areas where KCl is present. The main different between these two alloys, apart from minor differences in Cr and Al content, is the addition of Si in EF101. Si has previously been reported to greatly increase the corrosion resistance of stainless steels and FeCrAl alloys [18-29]. After transitioning into the secondary corrosion regime (after breakaway oxidation), Si has been shown to significantly reduce the corrosion rate [37, 38, 47]. Si is suggested to inhibit internal oxidation, which reduces the general corrosion rate. However, the prevention of internal oxidation also facilitates the formation of a corundum-type oxide healing layer which further reduces the corrosion rate. In addition to improving the secondary protection of an alloy, Si has been shown to improve the primary protection by enabling an alloy to resist breakaway oxidation in a corrosive environment. For stainless steels, Si has been reported to form a SiO2 layer which acts as a diffusion barrier, inhibiting the corrosion process [19, 22-25, 28, 48]. However, this is usually observed at temperatures above 650 °C and the formation of a SiO2 layer is expected to be very slow below this temperature.



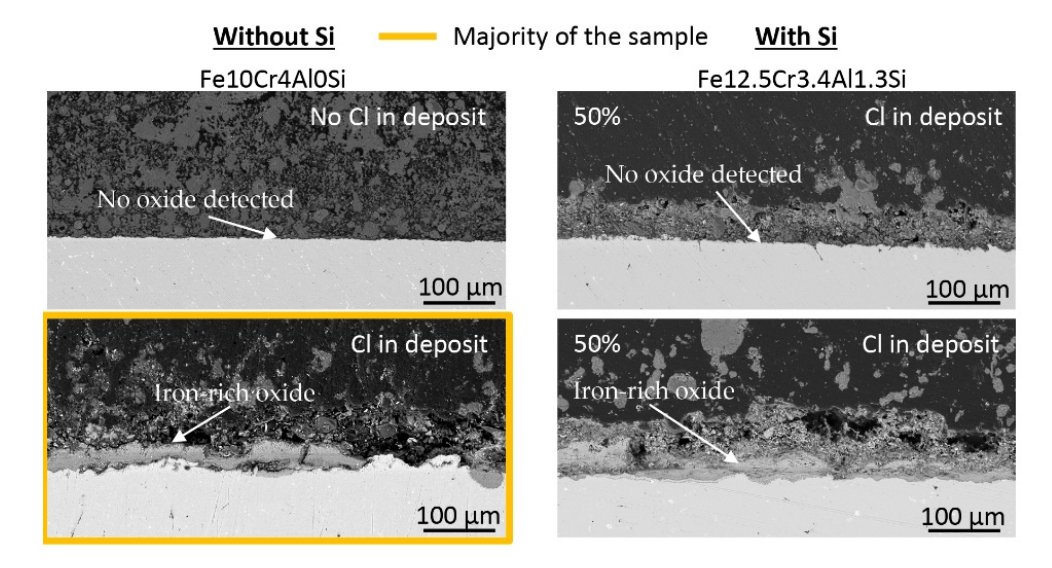


Figure 16: SEM-BSE images of the sample rings of the model alloy Fe10Cr4AlOSi (left) and EF101 (right) and the Fe10Cr4AlOSi alloy after the short-term exposures at a material temperature of 600 °C and at a position with low flue gas temperature.

Another Si-effect has been observed for FeCrAl alloys. Upon addition of Si, even relatively lean FeCrAl alloys (Cr content ≥ 5wt%) has been shown to resist breakaway oxidation in high-temperature environments (600 °C) containing water vapor [20, 29, 38]. Asokan et al. showed that the addition of Si significantly increased the Al content in the primary oxide, making it less sensitive towards the presence of water vapor [29]. In addition to providing a better protection against water vapor, a more Al-rich primary oxide scale may also increase the resistance towards alkali-salts, such as KCl and K2CO3. Persdotter et al. showed that a more highly alloyed FeCrAl alloy (Fe18Cr6Al), expected to quickly form an Al-rich oxide scale (due to high Al content), resisted breakaway oxidation in the presence of K₂CO₃ at 600 °C [3]. Israelsson et al. utilized the concept of pre-oxidation to preform a more Al-rich primary oxide scale before exposing the material to the presence of KCl [49, 50]. The pre-oxidized FeCrAl alloys were shown to be significantly better at resisting breakaway oxidation in small amounts of KCl. Similarly, this may explain the higher resistance of EF101 (and the other Sicontaining FeCrAl alloys) to Cl-containing deposits in the present work.

Among all the investigated materials, only one completely resisted breakaway oxidation under all conditions (position and material temperature), that is the EF101M-coated sample ring. The EF101M coating was able to resist the presence of Cl-containing deposit is all cases, as shown in the representative SEM image in Figure 17. Since the EF101M coating was enhanced in relation to its bulk version (higher Al and Si content, see section 4.2), this further demonstrates the beneficial effect of Si (and Al) and the importance of enabling rapid formation of an Al-rich primary oxide scale that may be able to resist the harsh environment of the boiler. While FeCrAl alloys generally cannot be used for pressure-bearing components, such as superheaters, due to the modest mechanical properties at these temperatures, the excellent performance of the EF101M coating demonstrates great



potential for utilizing this material class to reduce material degradation in biomassfired boilers.

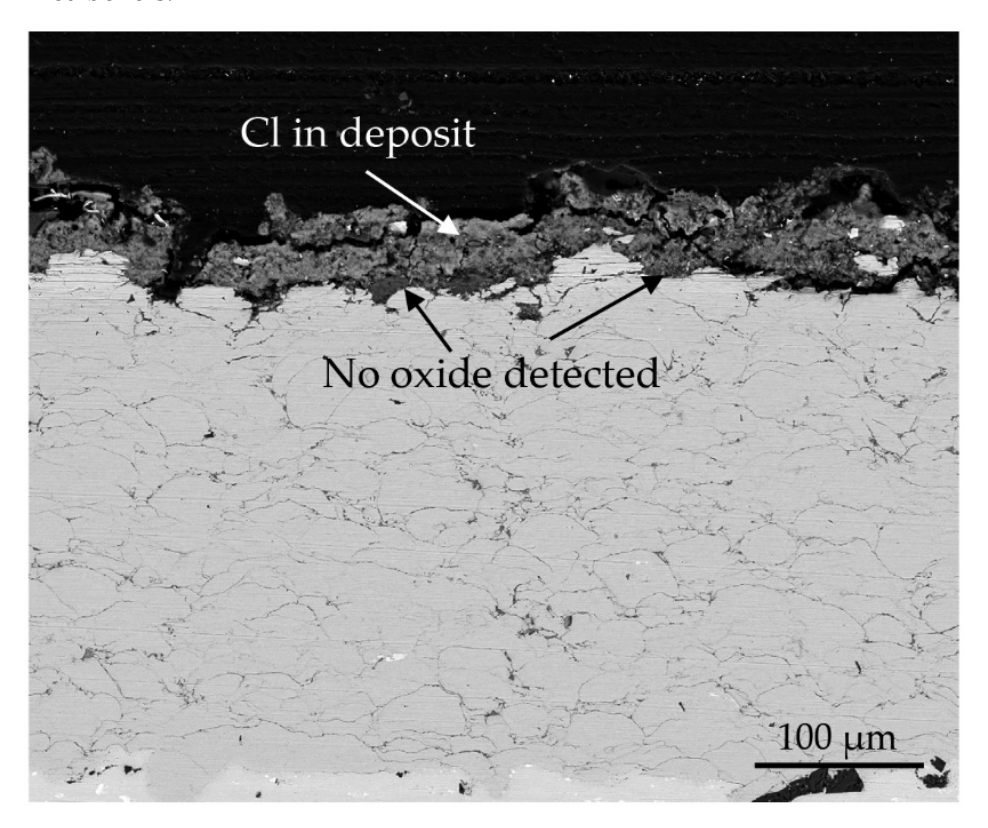


Figure 17: SEM-BSE image of a representative area of the sample ring coated with EF101 (enhanced) after the short-term exposure at a material temperature of 600 °C and at a position with low flue gas temperature.

As indicated by the IC measurements, the environment in the position of the corrosion probes was milder during the long-term exposure than for the short-term exposure. Expectedly, all alloys displayed less corrosion attack after 2000 hours of exposure than after 168 hours of exposure. This is also reflected by the extent of corrosion attack for the different alloys, displayed in Table 6. The stainless steels were shown to resist breakaway oxidation to a large extent as the majority of the sample ring surfaces remained in the primary corrosion regime with the exception being the 347H sample ring after exposure at a material temperature of 700 °C. Meanwhile, all FeCrAl alloys completely resisted breakaway oxidation and remained in the primary corrosion regime in all cases.

No Cl-containing species were detected in the deposit found on the sample rings. This is very different from the short exposure but expected if considering the very high S/Cl ratio given by the IC measurements. Since the FeCrAl alloys were shown to be fully resistant to the surrounding environment in the absence of Cl (during the short-term exposure), the excellent performance of the FeCrAl alloys during the long-term exposure is expected. During the short-term test, the lower material temperature (600 $^{\circ}$ C) resulted in a more corrosive deposit due to higher amounts of KCl. However, removing this factor (due to the high S/Cl ratio), the higher material temperature (700 $^{\circ}$ C) seems to elevate the corrosion attack (see stainless steels).



Table 6: Summary of data obtained from SEM analysis of all probe-samples after exposure for 2000 hours in the Asnæs boiler.

Alloy	600C	700C
347H	Primary	50/50
310HCbN	Primary	Majority Primary
Sanicro 25	Majority Primary	Majority Primary
EF101	Primary	Primary
Fe10Cr4Al0Si	Primary	Primary
Fe10Cr4Al1Si	Primary	Primary
Fe10Cr3Al2Si	Primary	Primary
347H with EF101M	Primary	Primary

6.3 FIXED INSTALLATIONS

The four sections of the three tubes (347H, 347HFG and 304HCu), welded into the tertiary superheater, as well as the 310HCbN tube endings were cast, cut and polished to enable SEM and LOM analysis (for further details, see section 4.3.2). The analyses were performed at four positions around the cut tube sections (including the leeward and windward sides) in order to investigate oxide type and thickness and material loss.

Wall thickness measurements on the exposed tube cross sections revealed minor deviation (<0.2 mm) from the nominal thicknesses shown in Table 1. However, all deviations were ascribed to variations in wall thickness due to tube manufacturing, and no indications of significant thinning due to corrosion or oxidation could be observed.

The removed tubes showed well adherent deposits of a light brown colour. Sections for metallography were removed near the steam outlet from the samples, Figure 18.



Figure 18 Appearance of the removed tubes and cutting of sections. Tube 23.5: 304HCu; Tube 24.5: 347HFG; Tube 25.5: 347H; Tube 25.5 right: 310HCbN



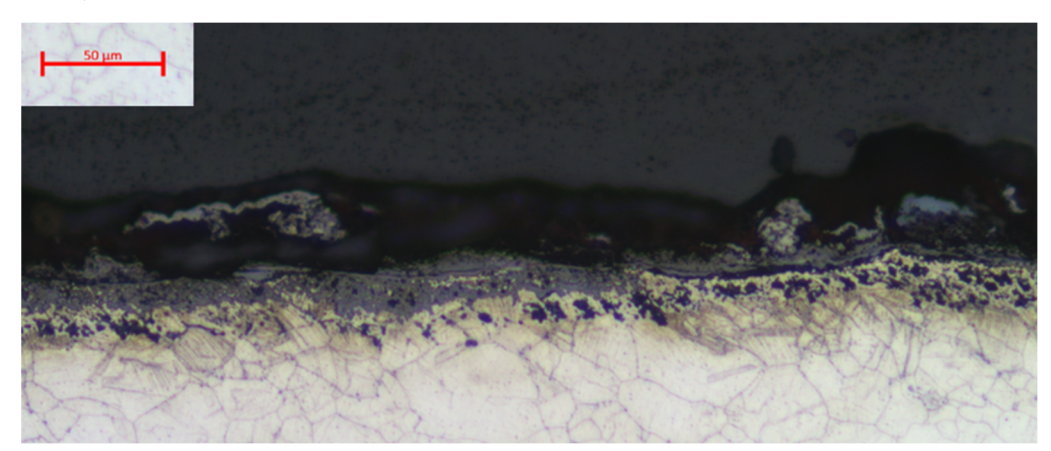
All investigated sections showed moderate corrosion attacks, which were found to be most clear on the windward side of the tubes. Secondary corrosion with formation of double layers could be observed in all steels. Also, internal corrosion (chromium leaching) was visible in all steels. Further, a zone with needle shaped precipitates were observed in all steels below the internal corrosion zone, Figure 20.

Thicknesses of the observed zones were estimated to compare with observations from other Danish biomass fired boilers, Table 7. The metal loss is taken as the sum of thicknesses of the inner corrosion layer and the internal corrosion.

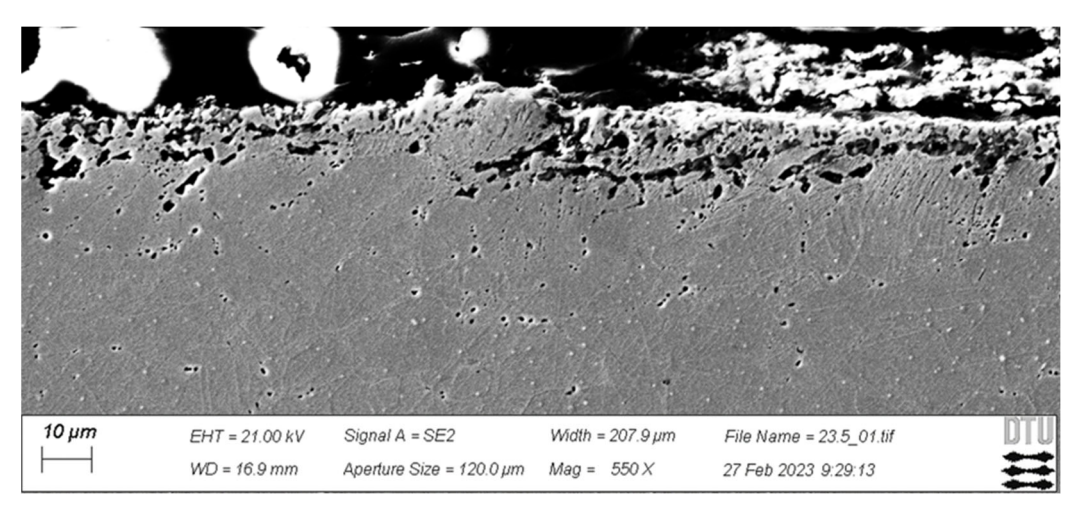
Table 7 Layer thicknesses observed on exposed tubes (windward side).

Material	Inner corrosion layer	Internal corrosion	Precipitation zone	Metal loss
304HCu	5-20 μm	5-15 μm	15-20 μm	10-35 μm
347HFG	5-15 μm	3-6 μm	3-6 μm	8-21 μm
347H	5-15 μm	15-20 μm	15-25 μm	20-35 μm
310HCbN	3-10 μm	10-20 μm	10-15 μm	13-30 μm

a) 304Cu







b) 347HFG

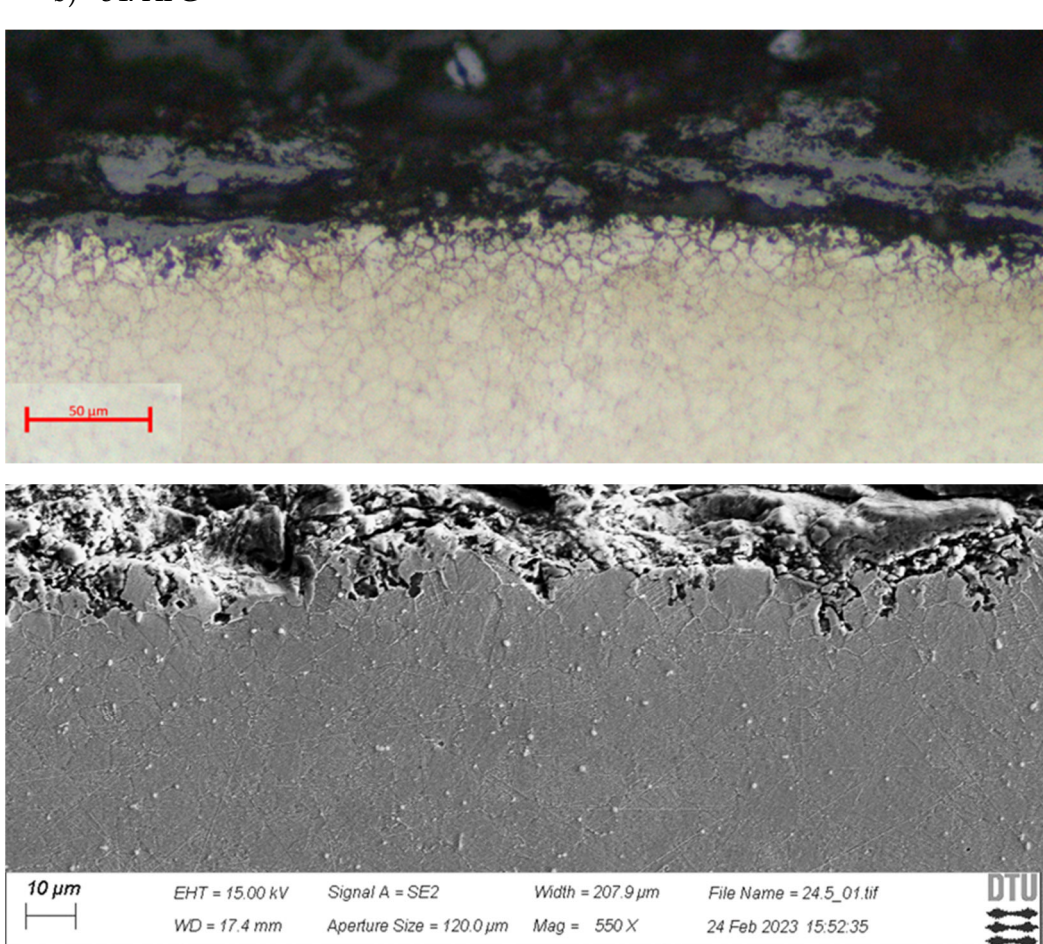


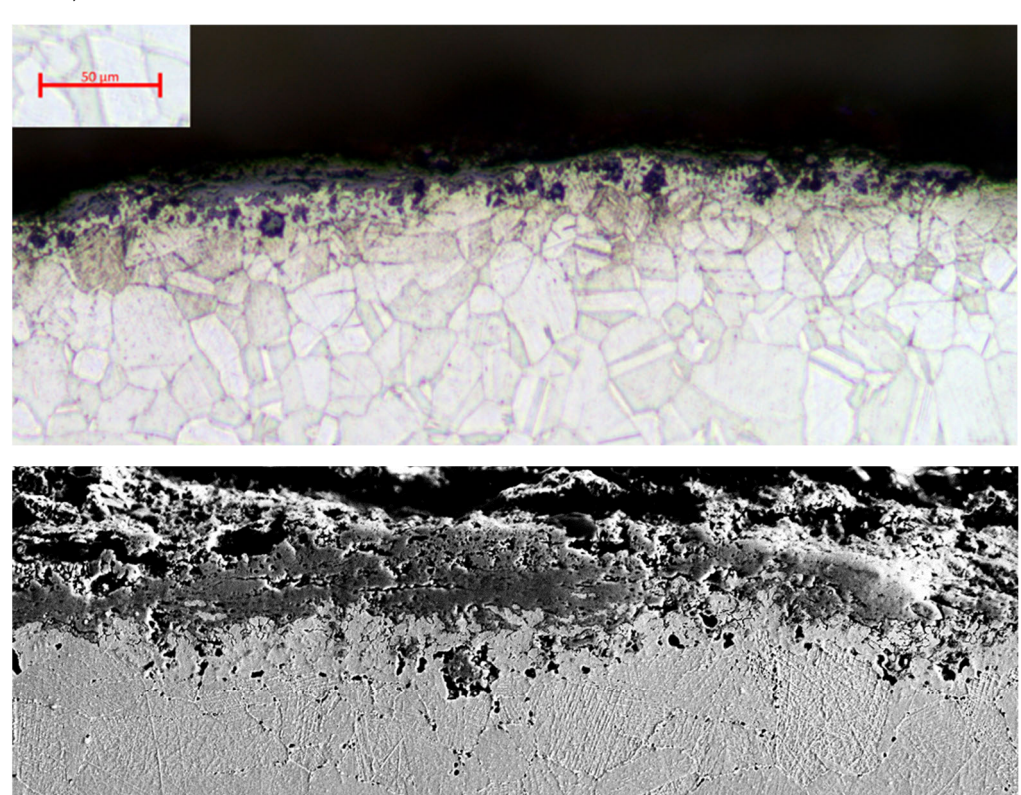
Figure 19 Light optical and SEM micrographs of corrosion attacks on the windward side of tubes. Ecthing Kallings reagent.



File Name = 25.5_01.tif

21 Feb 2023 10:38:19

c) 347H



d) 310HCbN

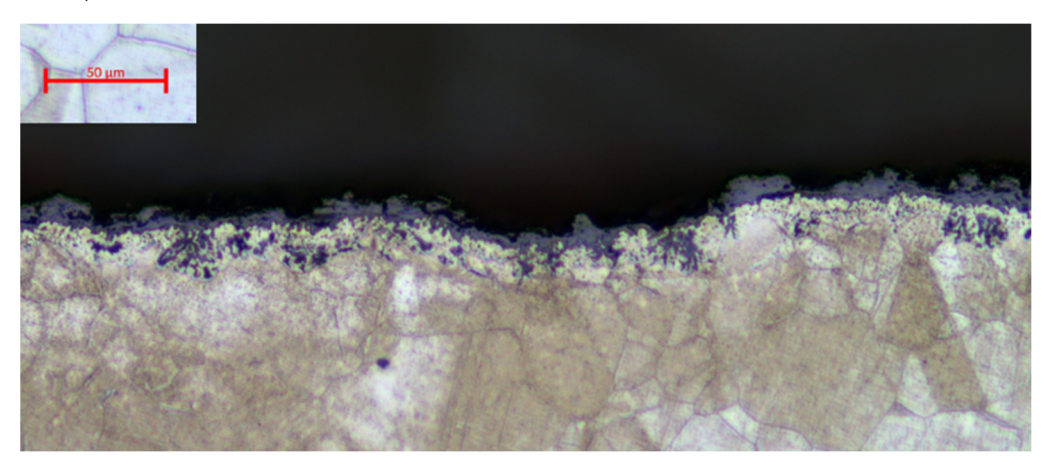
 $EHT = 12.00 \, kV$

WD = 10.6 mm

Signal A = SE2

Aperture Size = 120.0 µm Mag = 550 X

20 µm



 $Width = 207.9\,\mu m$



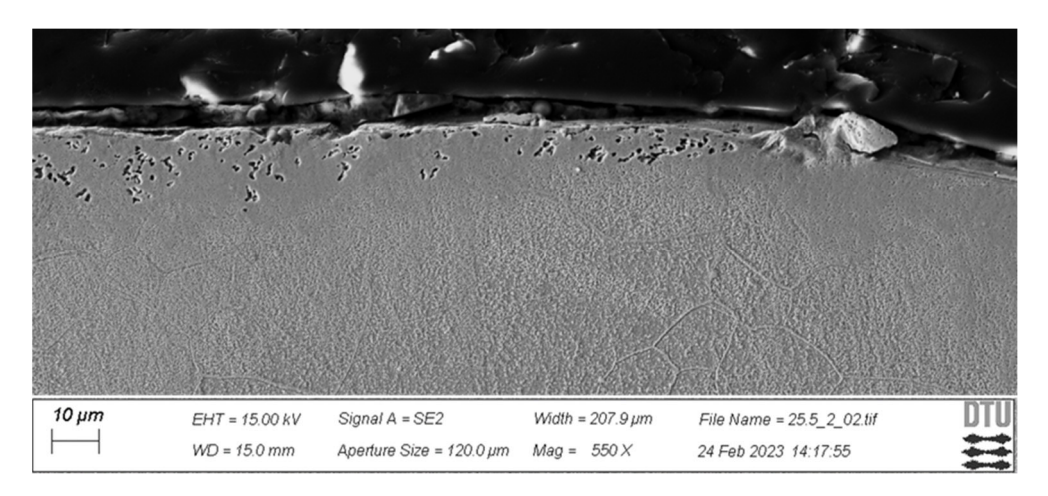


Figure 20 Light optical micrographs of corrosion attacks on the windward side of tubes. Ecthing Kallings reagent.

In the research project *Corrosion management in biomass firing* a large set of corrosion data from tube samples removed from Danish biomass fired power plants in the period 1997-2017 were collated into a database [51]. Systematic investigations of temperature data and corrosion rates allowed the creation of an empirical model to estimate materials loss as a function of the metal temperature. For straw firing the metal loss (average best case) of steels TP347H/TP347HFG is given as:

 $Kp (mm/1000h) = 8.84*10^{13} exp(-29046/T_{metal})$

Where K_P is a linear corrosion rate, and the metal temperature is in K.

Using this model on the exposure conditions for the present tubes, i.e. a metal temperature of 540°C, gives a corrosion rate of 27 μ m/1000h corresponding to a metal loss of 650 μ m in 23,850 hours.

As seen from Table 7 the observed metal losses in the present case are 20-80 times lower than for straw firing, which have high chloride content in flue gases. This clearly demonstrates effectiveness of the additives to remove chlorides.



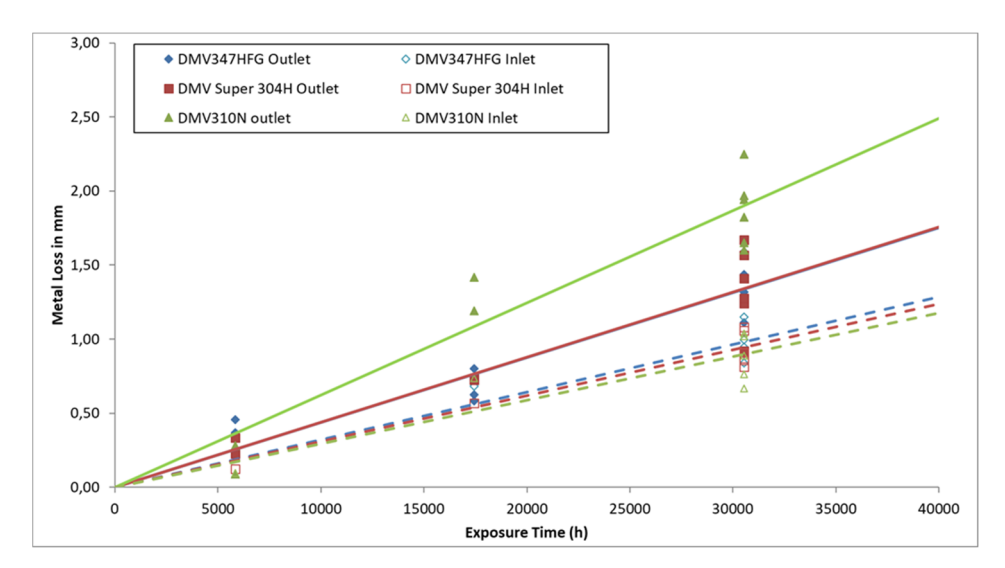


Figure 21. Metal loss in exposure tests at the suspension fired straw/wood pellet boiler Amager 1 [51]. There are slight differences between the materials, where 304HCu has higher corrosion (inner layer thickness) than the 347H/347HFG and 310HCbN, which show the lowest corrosion.

The internal corrosion is lowest in the 347HFG and rather similar in the 304HCu, 347H and 310HCbN. This leads to a lower metal loss in 347HFG than in the three other materials. Exposure tests with materials 347HFG, 304HCu and 310HCbN in the suspension fired straw/wood pellet boiler Amager 1 at steam outlet steam temperatures of 539-542°C, i.e., slightly higher metal temperatures than the present exposures, show a similar ranking of the materials corrosion resistance as the present experiments, Figure 21. Again, the low corrosion rates in the present samples as a result of additives are obvious.

Precipitation below the corrosion layers have been observed in Danish boilers, and detailed microstructure analysis in [51] show that in the temperature range for the present exposure test the precipitates are M₂₃C₆ carbides. They form on the fireside of boiler tubes during long term exposures to flue gases from coal firing as well as coal/biomass co-firing. However, in flue gases with high chloride content (such as straw firing without additives) carbide precipitates are rarely observed since they are quickly attacked by the chlorides. This attack of chromium rich precipitates is the mechanism for internal corrosion. The observation of clear carbide precipitates in the present exposure tests is thus another effect of the low chloride content as a result of additives.

6.4 OXIDATION SIMULATION

6.4.1 The primary corrosion regime (Chromia/Alumina)

The kinetic simulations of the corrosion process within the primary corrosion regime were performed at a material temperature of 600 and 700 $^{\circ}$ C for chromia (see Table 8 and Table 9) and at 900 $^{\circ}$ C for alumina (see Table 10) as described in section 5.



For the calculations of the chromia growth kinetics, the α - value was optimized based on experimental data (oxide thickness and grain size) from Hallström et al. [5] (600 °C) and Bataillou et al. [52] (700 °C). The accuracy of the obtained input data (grain size and α - value) was confirmed for the short exposure (168 hours) with experimental data from Tang et al. [53] (600 °C) and Jonsson et al. [54] (700 °C).

Among the investigated materials, 347H, 310HCbN and Sanicro 25 are expected to form a chromia scale within the primary corrosion regime. From the SEM analysis, chromia-formers were suggested to have retained the primary protection if no oxide could be detected with the assumption that the chromia scale would be too thin to detect with the utilized instrument/sample preparation (ion milling is usually necessary to reveal very thin oxide scale). The oxide thicknesses predicted with DICTRA for a material temperature of 600 °C shows that the chromia scale is in the 500 nanometer range even after 22000 hours of exposure, which confirms that the previously mentioned assumption applies. As expected, the growth rate of chromia increases at 700 °C but remains in the 600 nanometer range after 2000 hours of exposure. After 22000 hours, the chromia scale thickness has reached micrometer range but will still be difficult to detect with the utilized equipment. However, the SEM analysis of the fixed installations showed that different materials had transitioned into the secondary corrosion regime to a large extend and a more accurate prediction may be given my calculations based on iron oxidation (see next section).

Table 8: Input parameters and calculated values (oxide thickness) using DICTRA to predict oxidation kinetics of chromia at $600\,^{\circ}$ C.

Syste	T	Phases	Grain size	α	Time	Oxide thickness
m	(°C		(µm)		(hr)	(nm)
)					
Cr-O	600	bcc,	0.05	0.5	168	100
		corundum		9		
Cr-O	600	bcc,	0.13	0.5	2000	225
		corundum		9		
Cr-O	600	bcc,	0.3	0.5	22000	470
		corundum		9		

Table 9: Input parameters and calculated values (oxide thickness) using DICTRA to predict oxidation kinetics of chromia at 700 °C.

Syste	T	Phases	Grain	α	Time	Oxide thickness
m	(°C		size (µm)		(hr)	(nm)
)					
Cr-O	700	bcc,	0.15	0.52	168	300
		corundum		5		
Cr-O	700	bcc,	0.3	0.52	2000	600
		corundum		5		
Cr-O	700	bcc,	0.6	0.52	2200	1400
		corundum		5	0	



For the calculations of the alumina growth kinetics, the α - value was optimized based on experimental data (oxide thickness and grain size) from Liu et al. [9, 55, 56]. The accuracy of the obtained input data (grain size and α - value) was confirmed for the short exposure (168 hours) with experimental data from Engkvist et al. [57].

The alumina-formers investigated in this study, EF101, Fe10Cr4Al0Si, Fe10Cr4Al1Si and Fe10Cr3Al2Si, are expected to form transient alumina within the primary corrosion regime at both 600 and 700 °C due to the very slow formation of α -alumina at these temperatures (below 900 °C). Similar to the chromia-formers, the alumina-formers are suggested to have retained the primary protection if no oxide could be detected with SEM analysis because of the assumption that the transient alumina scale would be too thin to detect with the utilized instrument/sample preparation. The thicknesses of the alumina scale, predicted with DICTRA for a material temperature of 900 °C, shows that the alumina scale is in the 500-1000 nanometer range during short-term exposures (up to 2000 hours). Even after 22000 hours the alumina thickness is in the lower registry of the two micrometer range and would be difficult to detect without more advanced microscopy. The transient alumina formed at 600 and 700 °C have been shown to grow at a significantly lower rate. Asokan et al. [29] showed that an alloy similar to the Fe10Cr3Al2Si alloy formed a 50 nm thick transient alumina scale after 168 hours of exposure at 600 °C, i.e. significantly thinner than the alumina scale formed at 900 °C. Engkvist et al. [57] showed that the commercial FeCrAl alloy Kanthal AF formed a transient alumina scale with a thickness of 120 nm after 168 hours. Thus, the previously mentioned assumption, i.e. that if no oxide could be observed the alumina scale is too thin to be detected, applies for the alumina formers as well.



Table 10. Input parameters and calculated values (oxide thickness) using DICTRA to predict oxidation kinetics of alumina at 900 °C.

System	T (°C)	Phases	Grain size (μm)	α	Time (hr)	Oxide thickness (μm)
Al-O	900	fcc, corundum	0.185	0.655	168	0.5
Al-O	900	fcc, corundum	0.5	0.655	2000	1.0
Al-O	900	fcc, corundum	1.5	0.655	22000	2.0

The results from the Dictra calculations for the primary corrosion regime (chromia/alumina) are in agreement with previous literature and provides a reasonable explanation for the "absence" of an oxide scale in the cases where the primary protection has been retained. The high degree of retention of the primary protection for the materials exposed on the corrosion probes means that it is possible to predict the lifetime of these materials in the present environment using calculations based on the chromia/alumina systems.

6.4.2 The secondary corrosion regime (iron oxide)

The kinetic simulations of the corrosion process within the secondary corrosion regime were performed at a material temperature of 600 and 700 °C (see Table 11 and Table 12) as described in section 5.

For the calculations of the iron oxide growth kinetics, two alpha values were used, i.e. for corundum (representing hematite) and for spinel (representing both magnetite and inward-growing spinel). For the calculations at a material temperature of 600 °C, the α - values were optimized based on experimental data from Jonsson et al. [58]. Due to literature on iron oxidation at 700 °C, the α - values for calculations at this material temperature were optimized based on data extrapolated from Pujilaksono et al. [59] and Jonsson et al. [58]. The accuracy of the obtained input data for the calculations at 600 °C was confirmed with experimental data from Persdotter et al. [3] and Eklund et al. [20, 37]. The accuracy of the obtained input data for the calculations at 700 °C could not be confirmed due to insufficient literature data.

The predicted iron oxide thickness after 168 hours of exposure at 600 °C is 92 μm (see Table 11). The thickest recorded oxide among the samples exposed for 168 hours is 45 μm , observed on EF101 (see Figure 16). This indicates that none of the samples that has experienced breakaway oxidation at this temperature transitioned into the secondary corrosion regime in the initial stages of the probe exposure assuming a secondary protection kinetics in the same range as iron oxide. The same applies to the long-term exposure (2000 hours) at 600 °C for which the thickest recorded oxide is 16 μm , observed on Sanicro 25 (see Figure 46 in Appendix) while the calculated oxide thickness after 2000 hours is 320 μm . However, recent studies have shown that not all alloys that form an iron-rich oxide scale display the same oxide growth kinteics as pure iron, i.e. some iron-rich oxide scales are not purely limited by iron oxidation [3, 37, 38]. These studies showed that Fe-based alloys form a slower-growing iron-rich oxide when exceeding a



certain Cr concentration, which in turn varies depending on the concentrations of other elements, such as Al, Si [37, 38]. This has been connected to the inhibition of internal oxidation and the formation of a Cr-rich diffusion barrier (in the inward-growing scale), which is supported by thermodynamic equilibrium calculations. Ni has also been shown greatly affect the growth rate of the oxide scale after breakaway oxidation but less is known regarding the mechanism behind this effect [3]. Recent findings indicate that Ni promotes rapid formation of a Cr-rich corundum-type oxide scale that acts as a diffusion barrier [60]. The deviations from iron oxidation must be considered when interpreting the calculations and the calculated values can be seen as worst-case scenarios.

Table 11: Input parameters and calculated values (oxide thickness) using DICTRA to predict oxidation kinetics of iron oxide at 600 °C.

System	T (°C)	Phases	Grain size (μm)	α	Time (hr)	Oxide thickness (µm)
Fe-O	600	bcc, corundum, spinel	Spinel: 6 Corundum: 1	Spinel: 0.252 Corundum: 0.383	168	Spinel+Mag: 68 Corundum: 24
Fe-O	600	bcc, corundum, spinel	Spinel: 6 Corundum: 1	Spinel: 0.252 Corundum: 0.383	2000	Spinel+Mag: 236 Corundum: 84
Fe-O	600	bcc, corundum, spinel	Spinel: 8 Corundum: 2	Spinel: 0.252 Corundum: 0.383	22000	Spinel+Mag: 720 Corundum: 150

The predicted iron oxide thickness after 2000 hours of exposure at 700 °C is 229 μ m (see Table 12). The thickest recorded oxide among the samples exposed at 700 °C for 168 hours is 22 μ m, observed on 310HCbN (see Figure 47 in Appendix). The same applies to the long-term exposure (2000 hours) at 700 °C for which the highest recorded oxide thickness is 46 μ m, observed on 347H (see Figure 48 in Appendix) while the calculated oxide thickness (within the secondary corrosion regime) is 693 μ m. Similar to the data obtained at 600 °C, the observed oxide thickness indicates that the transition from the primary corrosion regime to the secondary corrosion regime (in the areas displaying iron-rich oxide) did not take place during the initial stages of the exposure but rather in the later stage. However, deviations from pure iron oxidation have to be considered at 700 °C as well. While increasing the temperature generally accelerates oxide growth rate, it also increases the diffusion rate of alloying elements such as Cr in the alloy, which could further facilitate the formation of a Cr-rich diffusion barrier.



Table 12: Input parameters and calculated values (oxide thickness) using DICTRA to predict oxidation kinetics of iron oxide at 700 $^{\circ}$ C.

System	T (°C)	Phases	Grain size (μm)	α	Time (hr)	Oxide thickness (μm)
Fe-O	700	bcc, corundum, spinel	Spinel:6 Corundum:1	Spinel: 0.252 Corundum: 0.383	168	Spinel+Mag: 153 Corundum: 76
Fe-O	700	bcc, corundum, spinel	Spinel:6 Corundum:1	Spinel: 0.252 Corundum: 0.383	2000	Spinel+Mag: 395 Corundum: 298



7 Conclusions

The main aim of this study is to increase the efficiency and flexibility of power generation from biomass-fired boilers to enable these power generating processes to compete with the corresponding fossil fuel base processes. To achieve this, two parallel approaches has been taken. The first part of the approach has been to investigate the performance of new materials, such as FeCrAl alloys, and compare these to the type of materials that are current in use in biomass-fired boilers. This has been done by means of carefully planned laboratory exposures, probe exposures within two different biomass-fired boilers and by investigating sample tubes installed in the tertiary superheater. The second part of the approach has been to generate new knowledge regarding corrosion simulations and how this may predict the performance of metallic components to give insight in the difference of lab/probe and fixed installed material in order to facilitate faster a materials selection process and increase the potential of biomass-fired power boilers.

The laboratory exposures provided an improved understanding of the performance of FeCrAl alloys in an environment simulating that of biomass-fired boilers. The relatively lean (low Cr and Al content) FeCrAl alloys were able to withstand breakaway oxidation in the presence of water vapor by adding minor amounts of Si to the alloy. Because of the relatively high-water vapor content in biomass-fired boilers, this finding is of great importance regarding reducing material degradation of metallic components in the boiler. The laboratory studies showed that the none of the alloys resisted breakaway oxidation in the presence of KCl in the lab investigation. This alkali salt is known to be one of the more corrosive species found in biomass-fired boilers and the results is in line with previous results. However, minor additions of Si were found to drastically reduce the oxide growth rate even after breakaway oxidation which provides a new approach/possibility to limit material degradation even in very harsh environments.

The probe exposures were performed in two different boilers (SKV402 and ASV06) and deposit tests were performed in connection to both exposures. The deposit tests showed that the chloride content was very low in both boilers (max 1.25 wt%) during the test periods but was the lowest in ASV06 (0.02 wt%). This indicates a very mild environment for both boilers compared to the laboratory exposures. Accordingly, the exposed sample rings displayed negligent material loss after both the short-term exposure (SKV402) and the long-term exposure (ASV06). The FeCrAl alloys generally performed better, especially at higher material temperature (700 °C) as they were able to retain the primary protection to a large extent limiting the material loss. The Si-containing FeCrAl alloys displayed the best performance in good agreement with the results from the laboratory exposures. The thermally sprayed EF101M sample ring retained the primary protection under all conditions which is promising for utilizing FeCrAl alloys without being limited by their pressure-bearing capabilities.

The test tubes (347H, 347HFG and 304Cu), installed in the tertiary superheater in the ASV06 boiler, remained installed for approximately 22 000 hours (not counting



the early commissioning of the boiler on low load). All test tubes, along with the 310HCbN tube endings, transitioned into the secondary corrosion regime during the operating lifetime. However, the material loss was negligible even after such a lengthy exposure. This opens a large flexibility regarding material choices in the boiler.

Thermodynamic calculations using DICTRA were performed in order to give insight in the difference of lab/probe and fixed installed material. These calculations were based on the formation or chromia, alumina and iron oxide. Input values, such as oxide grain size and oxide thickness, were obtained from the literature and was used to optimize and confirm the accuracy of the calculations. The calculated oxide thicknesses were compared to measured values from lab, probe exposures and fixed installations. The primary protection results are in very good agreement with the measured thicknesses and may in this context considered to be very protective. The predicted thickness for a primary protection is in the range of 1.5 μm after 22000h exposure at 700 °C and even expected to be thinner on the FeCrAl alloys.

The secondary protection, i.e. the oxide scale formed after breakaway oxidation was simulated with iron oxide. This provided indications on how long the materials had been within the secondary corrosion regime. However, while the predicted corrosion behaviour was accurate for some cases, the inaccuracy in other cases offered insights into necessary future improvements of the model, taking into consideration the formation of a healing layer after breakaway oxidation. The results indicate that the healing layer may be simulated as the primary protection (chromia or alumina) utilizing the exciting models. However, more work is needed in order to develop both the simulation models and the knowledge regarding the transition from a poor secondary protection to a good secondary protection. This new knowledge may aid not only in better predictions but also to develop/select corrosion resistant materials for harsh environments.



8 Goal fulfilment

The overall goals of the project has been achieved by generating new knowledge to facilitate the implementation of thermodynamic modelling in combination with activities to enable corrosion resistant materials for superheaters also at higher material temperatures. The currently utilized superheater materials has therefore be investigated in boiler exposures at varying temperatures (flue gas and metal) and compared with potential FeCrAl alloys, following a first ranking in the laboratory. This has provided an understanding as to the application and limitations of aluminum oxide forming materials as components for biomass-fired boilers. Thermodynamic calculations were performed in order to give insight in the difference of lab/probe and fixed installed material. The new knowledge may aid not only in better predictions but also to improve development/selecton of corrosion resistant materials for harsh environments.

The project results contribute to 2030 Swedish Energy Agency goals in the following way:

• Power generation from biomass contributes to a completely renewable and flexible electrical system by providing planned power generation. *The results from the scale up investigation lab-probe-fixed installed material enables faster development and a more flexible system in the future.*

This goal is considered fulfilled.

Materials that allow higher steam data of conversion of biofuels to
electricity and heat enables a resource-efficient and cost-effective manner
with minimal environmental impact. The results show the potential in
material development/selection to increase the efficiency in power generation from
biomass trough higher material temperatures.

This goal is considered fulfilled.

The collaboration and continuous exchange of knowledge within the
project includes the whole value chain. The research within the project has
been in the research front implementing novel methods e.g. state of the art
thermodynamic modelling securing that Swedish research in this field
continues to maintain a high international level.

This goal is considered fulfilled.

The scientific goals of the project:

• Determine the applicability and limitations of aluminum oxide forming materials for improved biomass conversion effect, as well as their comparison with existing materials. The newly developed FeCrAl alloys has been investigated in lab/probe exposers providing knowledge regarding the applicability and limitations of aluminum oxide forming materials for improved biomass conversion effect. The potential of applying a FeCrAl alloy as a coating was also investigated to gage the possibility of utilizing FeCrAl alloys without the



limitations of their pressure-bearing capabilities. The results have been compared to existing materials.

This goal is considered fulfilled.

 Implement thermodynamic-kinetic modelling of oxidation in complex environments. This has been performed through oxidation kinetic simulations. The new knowledge generated from the previous point has been utilized to implement thermodynamic-kinetic modelling of the oxidation process of key components in the boilers. The calculations provided valuable information regarding how long the different types of materials remain within the different corrosion regimes (primary and secondary).

This goal is considered fulfilled.

• Scale up lab-probe-fixed installation tests - predict impact of e.g. material and temperature on lifetime of key components. *This has been performed through a combined investigation of lab-probe-fixed installed material and oxidation simulations.*

This goal is considered fulfilled.

 The research within the project is in the research front implementing novel methods as e.g. state-of-the-art thermodynamic modelling. The aim is to publish the work in scientific journals and produce PhD students within the project.

Academic goals of the project:

Academic thesis - two

Journal publications - two

The work has been a part of Johan Eklunds PhD thesis (2021) and will be implemented in Vicent Ssenteza Licentiate thesis (2023). The work is in addition in the process of been summarized in two journal publications.

This goal is considered fulfilled.



9 Suggestions for future work

This project has explored ways to increase the efficiency and predictability/flexibility of power generation from biomass. Two different pathways have been investigated in the project, i.e., material development and oxidation simulations, through a combination of lab investigations, probe exposures as well as fixed installed material in a commercial boiler.

The results have enlightened various aspects and possibilities. The two strategies go hand in hand and shows the potential with the new materials, i.e. FeCrAl alloys where a very thin oxide scale was observed after 2000h at a material temperature of 700 \circ C in the boiler as well as the possibility to extrapolate these results. Utilizing the simulations this would correspond to an oxide scale in the 2 μ m range after 22 000h. However, the results obtained within the project have also raised many suggestions for further studies. Especially, if the questions addressed in the project should be scientifically answered a more extensive exposure matrix needs to be performed, investigating the different steps more thoroughly. Other aspects that may be further investigated:

- It would be necessary to further investigate the exposure temperature for the FeCrAl alloys as the higher temperature was limited to the probe exposure in this case.
- Investigate more challenging fuels/environments as well as variations in environment/fuel in order to better understand the impact of environment on the link between lab investigations, probe exposures as well as fixed installed material in a commercial boiler.
- Develop the oxidation simulations to include the reformation of a protective scale, i.e. a healing layer.
- Investigate the alloy composition/exposure environment impact on the formation of a good secondary protection in harsh environments.

Generally, the thermodynamic/kinetic calculations could provide improved lifetime predictions of boiler components. This would aid not only the efficiency and predictability but also aid the selection/development of corrosion resistant materials for these environments and applications.



10 References

- 1. Pettersson, J., et al., *KCl Induced Corrosion of a 304-type Austenitic Stainless Steel at 600°C; The Role of Potassium.* Oxidation of Metals, 2005. **64**(1): p. 23-41.
- 2. Jonsson, T., et al., *High-Temperature Oxidation of FeCr(Ni) Alloys: The Behaviour After Breakaway.* Oxidation of Metals, 2017. **87**(3-4): p. 333-341.
- 3. Persdotter, A., et al., Beyond Breakaway Corrosion Influence of Chromium, Nickel and Aluminium on Corrosion of Iron-based Alloys at 600 °C. Corrosion Science, 2020: p. 108961.
- 4. Larsson, H., et al., *Oxidation of iron at 600 °C experiments and simulations*. Materials and Corrosion, 2016. **68**(2): p. 133-142.
- 5. Hallström, S., et al., *High temperature oxidation of chromium: Kinetic modeling and microstructural investigation.* Solid State Ionics, 2013. **240**: p. 41-50.
- 6. Bigdeli, S., et al., Strategies for high-temperature corrosion simulations of Fe-based alloys using the Calphad approach Part I, in Journal of phase equilibria and diffusion.

 Submitted.
- 7. Kofstad, P., *High temperature corrosion*. 1988, London; New York, N.Y.: Elsevier applied science.
- 8. Götlind, H., et al., *The Effect of Water Vapor on the Initial Stages of Oxidation of the FeCrAl Alloy Kanthal AF at 900* °C. Oxidation of Metals, 2007. **67**(5): p. 251-266.
- 9. Liu, F., et al., TEM investigation of the oxide scales formed on a FeCrAIRE alloy (Kanthal AF) at 900°C in dry O2 and O2 with 40% H2O. Materials at High Temperatures, 2005. **22**(3-4): p. 521-526.
- 10. Israelsson, N., et al., *KCl-Induced Corrosion of the FeCrAl Alloy Kanthal* ® *AF at 600* °C and the Effect of H2O. Oxidation of Metals, 2015. **83**(1): p. 1-27.
- 11. Josefsson, H., et al., *Oxidation of FeCrAl alloys at 500–900°C in dry O2*. Materials and Corrosion, 2005. **56**(11): p. 801-805.
- 12. Asteman, H., et al., Oxidation of stainless steel in H2O/O-2 environments Role of chromium evaporation, in High Temperature Corrosion and Protection of Materials 6, Prt 1 and 2, Proceedings, P. Steinmetz, et al., Editors. 2004, Trans Tech Publications Ltd: Zurich-Uetikon. p. 775-782.
- 13. Pettersson, J., et al., *The Effects of KCl, K2SO4 and K2CO3 on the High Temperature Corrosion of a 304-Type Austenitic Stainless Steel.* Oxidation of Metals, 2011. **76**(1): p. 93-109.
- 14. Pettersson, C., L.G. Johansson, and J.E. Svensson, *The Influence of Small Amounts of KCl(s) on the Initial Stages of the Corrosion of Alloy Sanicro 28 at 600 °C.* Oxidation of Metals, 2008. **70**(5): p. 241-256.
- 15. Karlsson, S., et al., *Alkali Induced High Temperature Corrosion of Stainless Steel: The Influence of NaCl, KCl and CaCl2.* Oxidation of Metals, 2012. **78**(1): p. 83-102.
- 16. Li, Y.S., Y. Niu, and M. Spiegel, *High temperature interaction of Al/Si-modified Fe–Cr alloys with KCl.* Corrosion Science, 2007. **49**(4): p. 1799-1815.
- 17. Sui, J.X., et al., The Effects of KCl, NaCl and K2CO3 on the High-Temperature Oxidation Onset of Sanicro 28 Steel. OXIDATION OF METALS, 2016. **85**(5-6): p. 565-598.
- 18. Basu, S.N. and G.J. Yurek, Effect of alloy grain size and silicon content on the oxidation of austenitic Fe-Cr-Ni-Mn-Si alloys in pure O2. Oxidation of Metals, 1991. **36**(3): p. 281-315.
- 19. Dunning, J., D. Alman, and J.J.O.o.M. Rawers, *Influence of silicon and aluminum additions on the oxidation resistance of a lean-chromium stainless steel.* 2002. **57**(5-6): p. 409-425.
- 20. Eklund, J., et al., *The influence of silicon on the corrosion properties of FeCrAl model alloys in oxidizing environments at* 600 °C. Corrosion Science, 2018. **144**: p. 266-276.



- 21. Kiamehr, S., et al., *KCl-induced high temperature corrosion of selected commercial alloys*. Materials and Corrosion, 2016. **67**(1): p. 26-38.
- 22. Mikkelsen, L., S. Linderoth, and J. Bilde-Sørensen. *The effect of silicon addition on the high temperature oxidation of a Fe-Cr alloy*. in *Materials Science Forum*. 2004. Trans Tech Publ.
- 23. Nguyen, T.D., J. Zhang, and D.J. Young, Effects of Silicon on High Temperature Corrosion of Fe–Cr and Fe–Cr–Ni Alloys in Carbon Dioxide. Oxidation of Metals, 2014. **81**(5): p. 549-574.
- 24. Nguyen, T.D., J. Zhang, and D.J. Young, Effects of Silicon and Water Vapour on Corrosion of Fe–20Cr and Fe–20Cr–20Ni Alloys in CO2 at 650 °C. Oxidation of Metals, 2017. 87(3): p. 541-573.
- 25. Pettersson, R., et al., Cyclic oxidation performance of silicon-alloyed stainless steels in dry and moist air. 2005. **40**(3): p. 211-216.
- 26. RADAVICH, J.F., Effect of Silicon on High Temperature Oxidation Of Stainless Steels. CORROSION, 1959. **15**(11): p. 73-77.
- 27. Sand, T., et al., *Exploring the Effect of Silicon on the High Temperature Corrosion of Lean FeCrAl Alloys in Humid Air.* Oxidation of Metals, 2021. **95**(3): p. 221-238.
- 28. Wouters, Y., et al., Oxygen and Water Vapour Oxidation of 15Cr Ferritic Stainless Steels with Different Silicon Contents. Materials Science Forum, 2004. **461-464**: p. pp. 839-848.
- 29. Asokan, V., et al., *The influence of Si on the primary protection of lean FeCrAl model alloys in O2 and O2+H2O at 600 °C—A microstructural investigation.* Corrosion Science, 2021. **179**: p. 109155.
- 30. Asteman, H., J.E. Svensson, and L.G. Johansson, *Oxidation of 310 steel in H2O/O2 mixtures at 600 °C: the effect of water-vapour-enhanced chromium evaporation*. Corrosion Science, 2002. **44**(11): p. 2635-2649.
- 31. Asteman, H., et al., Influence of Water Vapor and Flow Rate on the High-Temperature Oxidation of 304L; Effect of Chromium Oxide Hydroxide Evaporation. Oxidation of Metals, 2000. 54(1): p. 11-26.
- 32. Halvarsson, M., et al., *Microstructural investigation of the breakdown of the protective oxide scale on a 304 steel in the presence of oxygen and water vapour at 600°C.* Corrosion Science, 2006. **48**(8): p. 2014-2035.
- 33. Tang, J.E., et al., Investigation of FIB-thinned TEM cross-sections of oxide scales formed on type 310 steel at 600°C in water vapour-containing oxygen atmospheres. Materials at High Temperatures, 2007. **24**(1): p. 27-55.
- 34. Kiamehr, S., et al., *KCl-induced high temperature corrosion of selected commercial alloys*. Materials and Corrosion, 2015. **67**(1): p. 26-38.
- 35. Li, Y.S., M. Spiegel, and S. Shimada, *Effect of Al/Si addition on KCl induced corrosion of 9% Cr steel*. Materials Letters, 2004. **58**(29): p. 3787-3791.
- 36. Jonsson, T., et al., Oxidation After Breakdown of the Chromium-Rich Scale on Stainless Steels at High Temperature: Internal Oxidation. Oxidation of Metals, 2016. **85**(5): p. 509-536.
- 37. Eklund, J., et al., Secondary corrosion protection of FeCr(Al) model alloys at 600 °C The influence of Cr and Al after breakaway corrosion. Corrosion Science, 2021. **189**: p. 109584.
- 38. Eklund, J., et al., *High temperature corrosion behavior of FeCrAlSi model alloys in the presence of water vapor and KCl at 600 °C The influence of Cr content.* Corrosion Science, 2022. **198**: p. 110114.
- 39. Eklund, J., et al., *The long-term corrosion behavior of FeCrAl(Si) alloys after breakaway oxidation at 600* °C. To be published (2022).
- 40. Karlsson, S., et al., A Laboratory Study of the in Situ Sulfation of Alkali Chloride Rich Deposits: Corrosion Perspective. Energy & Fuels, 2016. **30**(9): p. 7256-7267.



- 41. Jonsson, T., et al., The Influence of KCl on the Corrosion of an Austenitic Stainless Steel (304L) in Oxidizing Humid Conditions at 600 °C: A Microstructural Study. Oxidation of Metals, 2009. 72(3): p. 213-239.
- 42. Krause, H., et al., Corrosion and Deposits from Combustion of Solid Waste—Part VI: Processed Refuse as a Supplementary Fuel in a Stoker-Fired Boiler. 1979.
- 43. Salmenoja, K. and K. Makela. *Prevention of superheater corrosion in the combustion of biofuels*. in *CORROSION 2000*. 2000. OnePetro.
- 44. Robinson, A.L., H. Junker, and L.L. Baxter, *Pilot-scale investigation of the influence of coal–biomass cofiring on ash deposition*. Energy & Fuels, 2002. **16**(2): p. 343-355.
- 45. Bradley, R.S. and P. Volans, *Rates of Evaporation. VI. The Vapour Pressure and Rate of Evaporation of Potassium Chloride.* Proceedings of the Royal Society of London. Series A, Mathematical and Physical Sciences, 1953. **217**(1131): p. 508-523.
- 46. Phother-Simon, J., T. Jonsson, and J. Liske, *Continuous KCl addition in high temperature exposures of 304 L A way to mimic a boiler environment*. Corrosion Science, 2020. **167**: p. 8.
- 47. Eklund, J., et al., Field exposure of FeCrAl model alloys in a waste-fired boiler at 600°C: The influence of Cr and Si on the corrosion behaviour. 2019. **70**(8): p. 1476-1485.
- 48. Jonsson, T., et al., Microstructural Investigation of the Effect of Water Vapour on the Oxidation of the Si-Containing FeCrNi Steel 353MA at 900 (Degree Sign) C in Oxygen. Meeting Abstracts, 2006. MA2006-02(18): p. 949.
- 49. Israelsson, N., *High Temperature Oxidation and Chlorination of FeCrAl Alloys*. 2014, Chalmers University of Technology.
- 50. Israelsson, N., et al., *KCl-Induced Corrosion of an FeCrAl Alloy at 600 °C in O2 + H2O Environment: The Effect of Pre-oxidation.* Oxidation of Metals, 2015. **83**(1): p. 29-53.
- 51. DTU Mechanical Engineering and DONG Energy (Ørsted), *Corrosion management in biomass firing*. ForskEL 2015-1-12289 (2019). Available on request from jhald@dtu.dk.
- 52. Bataillou, L., et al., *Growth kinetics and characterization of chromia scales formed on Ni–* 30Cr alloy in impure argon at 700° C. Oxidation of Metals, 2020. **93**(3): p. 329-353.
- 53. Eu Tang, J., et al., *The microstructure of the base oxide on 304L steel*. Micron, 2001. **32**(8): p. 799-805.
- 54. Jonsson, T., et al., *Microstructural investigation of the effect of water vapour on the oxidation of alloy 353 MA in oxygen at 700 and 900°C.* Materials at High Temperatures, 2005. **22**(3-4): p. 231-243.
- 55. Liu, F., et al., Early stages of the oxidation of a FeCrAlRE alloy (Kanthal AF) at 900°C: A detailed microstructural investigation. Corrosion Science, 2008. **50**(8): p. 2272-2281.
- 56. Liu, F., et al., TEM Investigation of the Microstructure of the Scale Formed on a FeCrAlRE Alloy at 900 °C: The Effect of Y-rich RE Particles. Oxidation of Metals, 2010. 74(1): p. 11-32.
- 57. Engkvist, J., et al., *Oxidation of FeCrAl foils at 500–900°C in dry O2 and O2 with 40% H2O.* Materials at High Temperatures, 2009. **26**(2): p. 199-210.
- 58. Jonsson, T., et al., Oxidation of Fe–10Cr in O2 and in O2+H2O environment at 600°C: A microstructural investigation. Corrosion Science, 2013. **75**: p. 326-336.
- 59. Pujilaksono, B., et al., *Oxidation of iron at 400–600°C in dry and wet O2*. Corrosion Science, 2010. **52**(5): p. 1560-1569.
- 60. Ssenteza, V., et al., High temperature corrosion of FeCr(Ni, Al) alloys in KCl at 600 °C: Microstructural evolution after breakaway oxidation. To be published.



11 Appendix

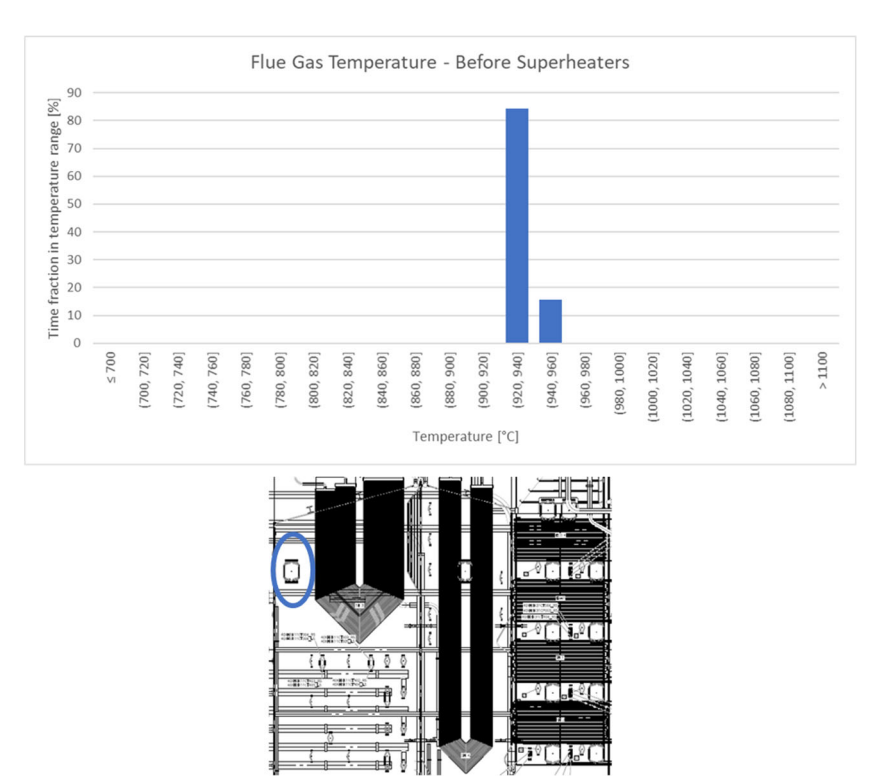
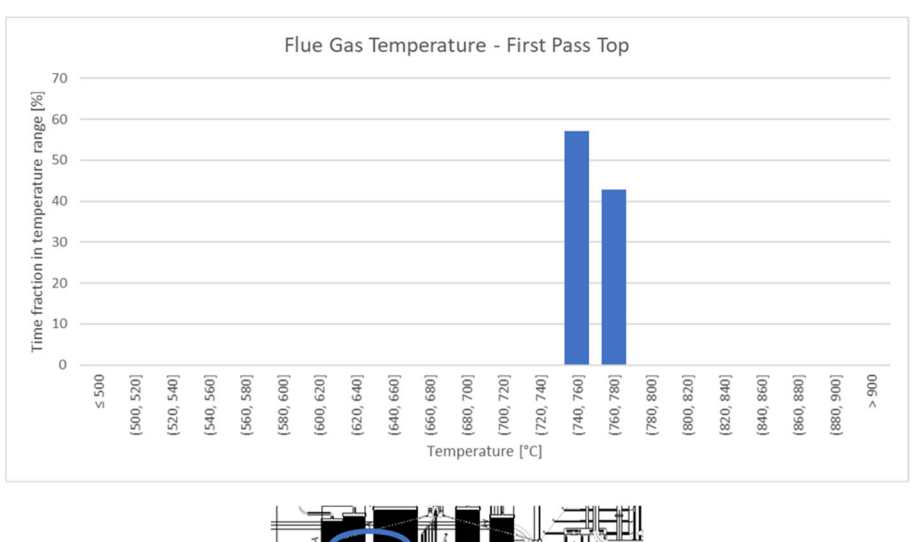


Figure 22: Diagram showing the flue gas temperature before superheaters during the deposit test in the SKV402 boiler with schematic showing the position at which the temperature was measured.





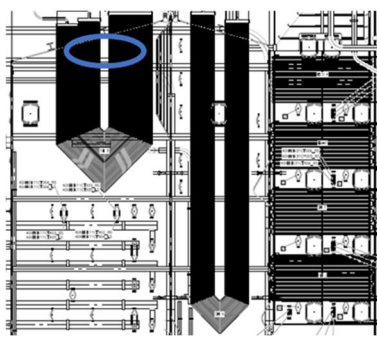
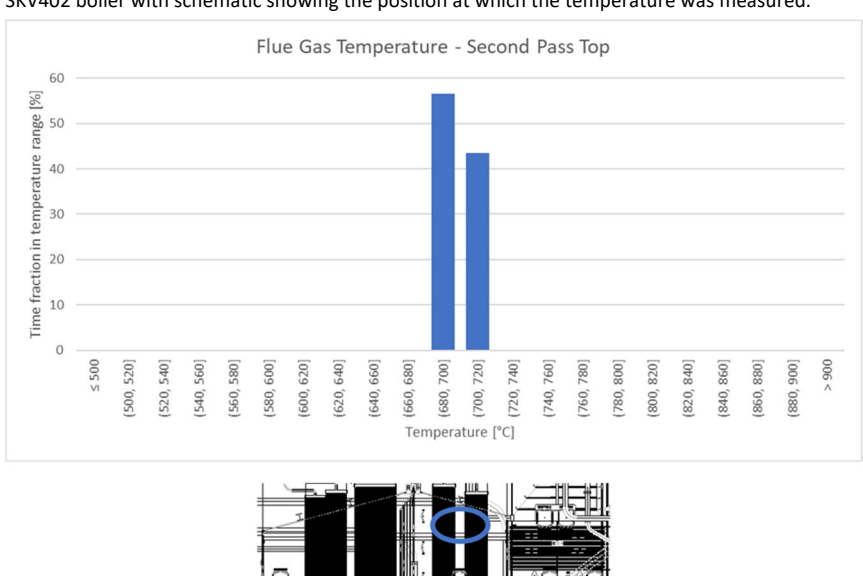


Figure 23: Diagram showing the flue gas temperature at the top of the first pass during the deposit test in the SKV402 boiler with schematic showing the position at which the temperature was measured.



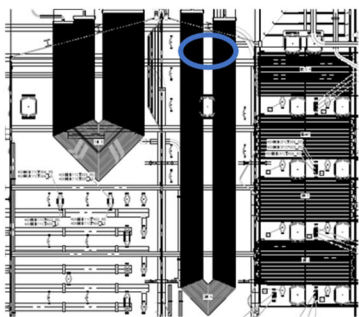


Figure 24: Diagram showing the flue gas temperature at the top of the second pass during the deposit test in the SKV402 boiler with schematic showing the position at which the temperature was measured.



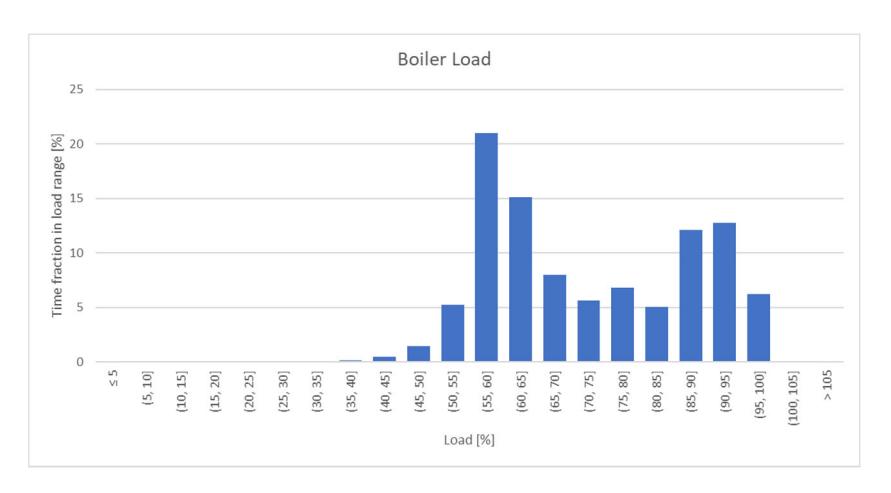


Figure 25: Diagram showing the boiler load during the corrosion test in the SKV402 boiler.

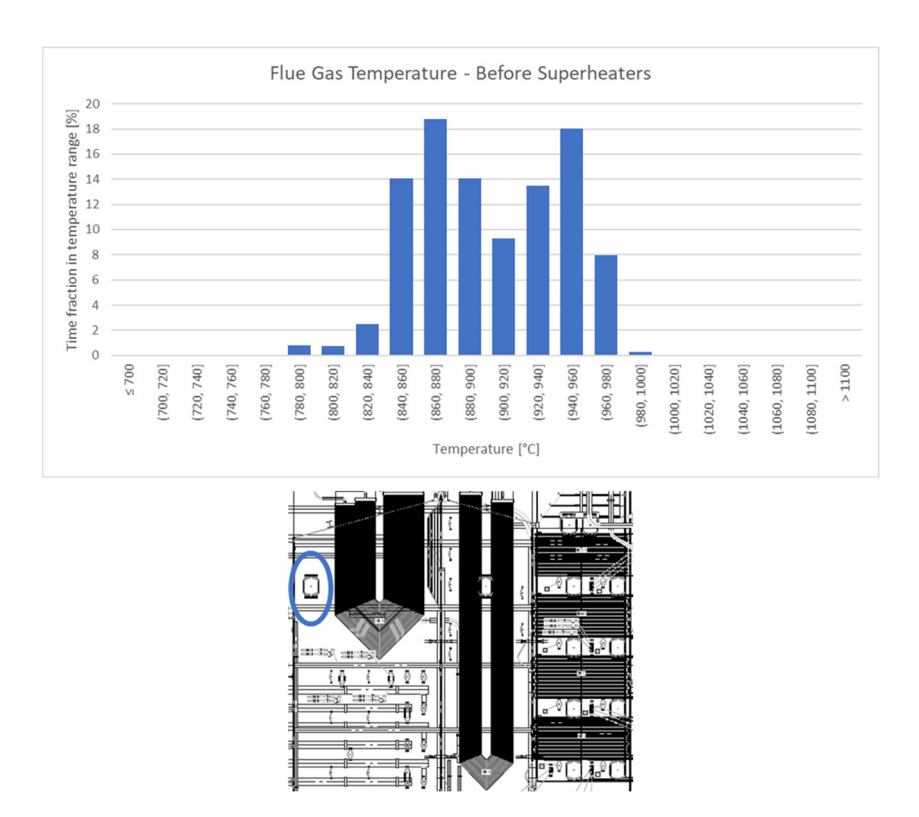


Figure 26: Diagram showing the flue gas temperature before superheaters during the corrosion test in the SKV402 boiler with schematic showing the position at which the temperature was measured.



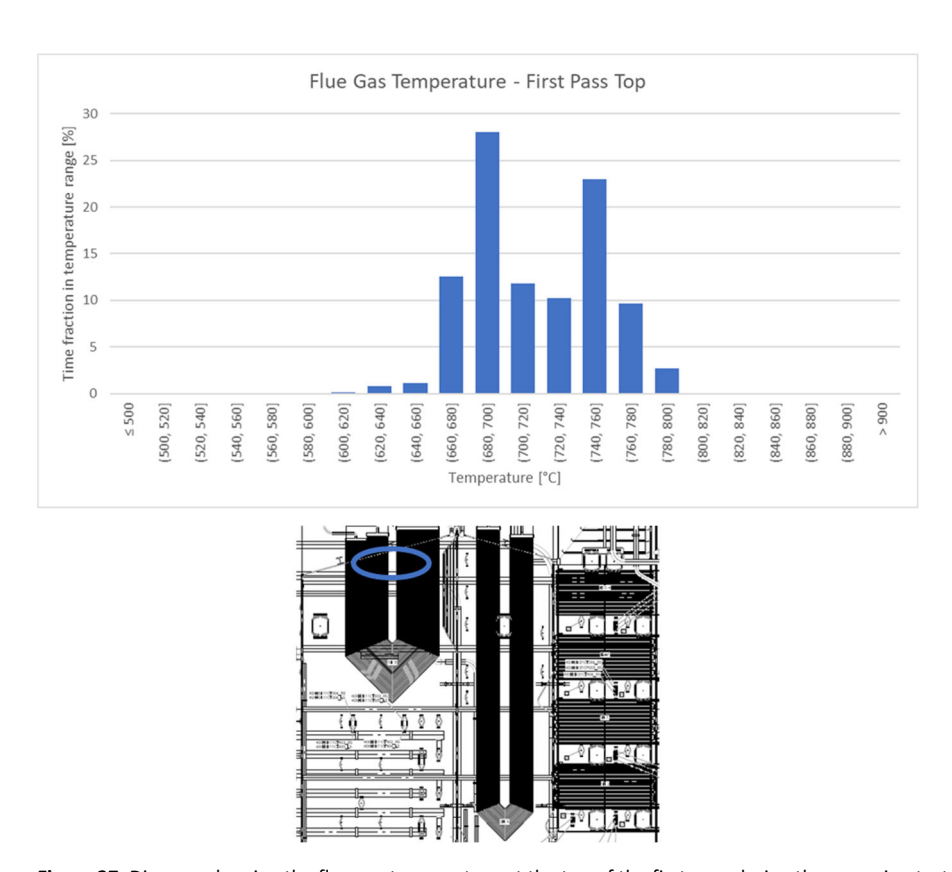


Figure 27: Diagram showing the flue gas temperature at the top of the first pass during the corrosion test in the SKV402 boiler with schematic showing the position at which the temperature was measured.

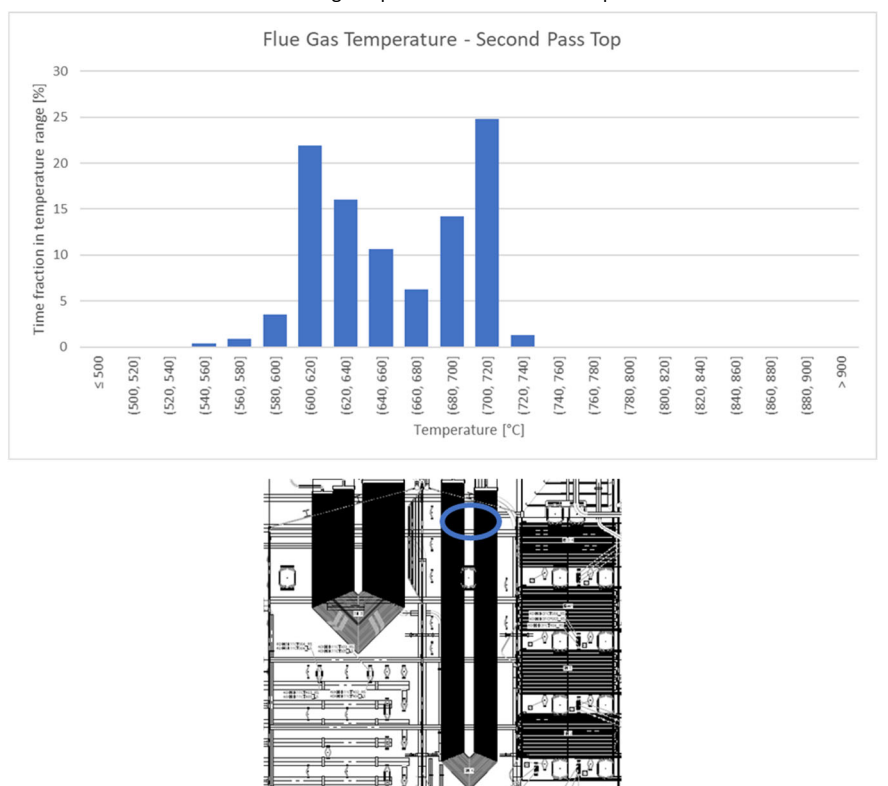


Figure 28: Diagram showing the flue gas temperature at the top of the second pass during the corrosion test in the SKV402 boiler with schematic showing the position at which the temperature was measured.



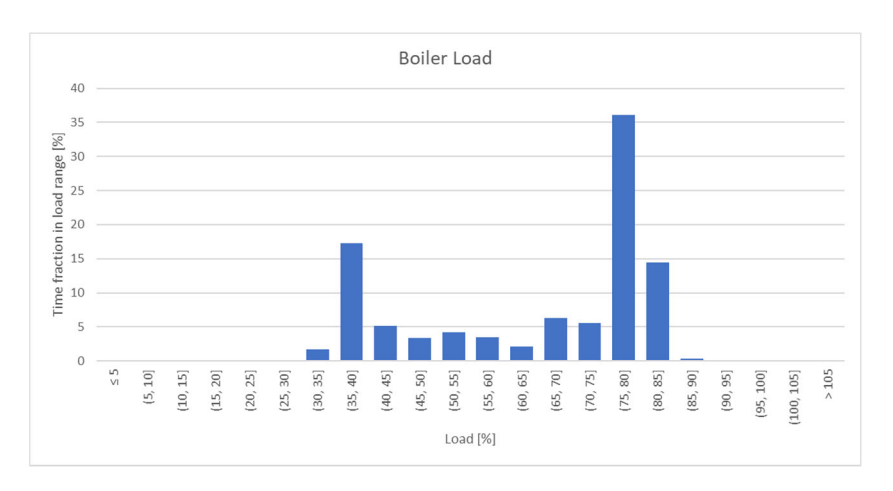
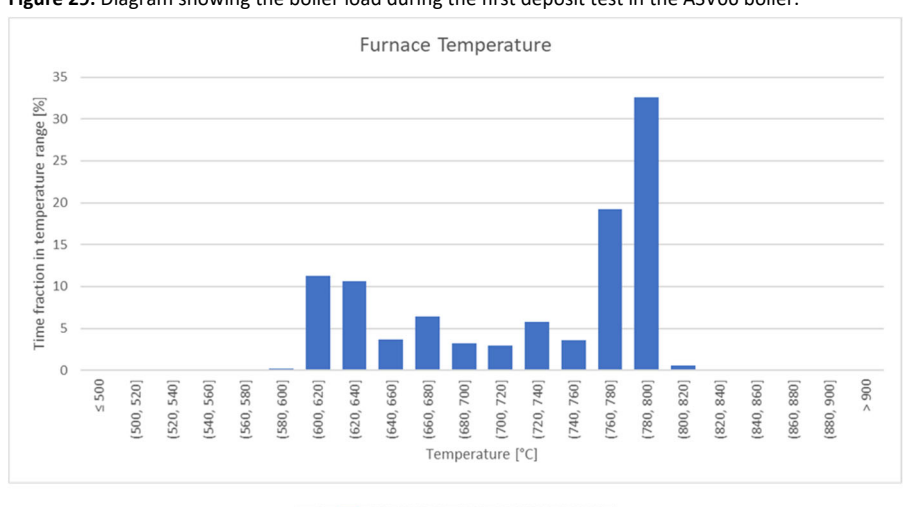


Figure 29: Diagram showing the boiler load during the first deposit test in the ASV06 boiler.



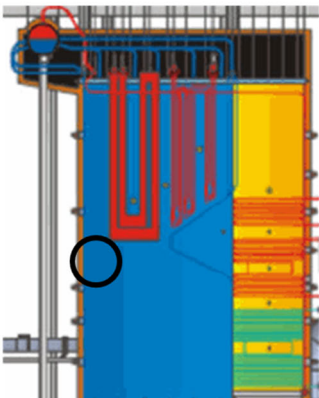
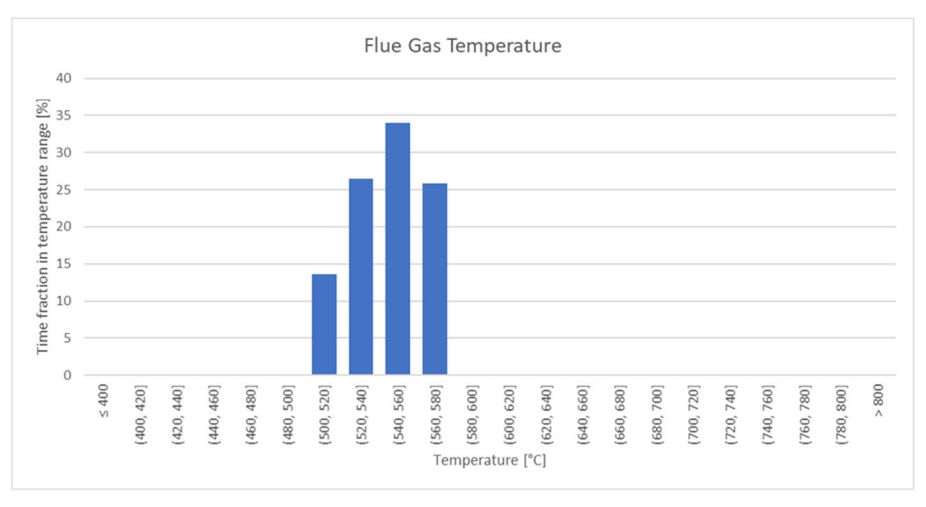


Figure 30: Diagram showing the furnace temperature during the first deposit test in the ASV06 boiler. The schematic shows the position at which the temperature was measured.





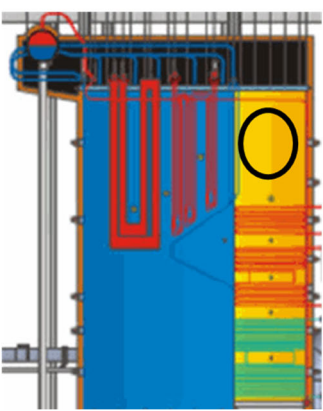
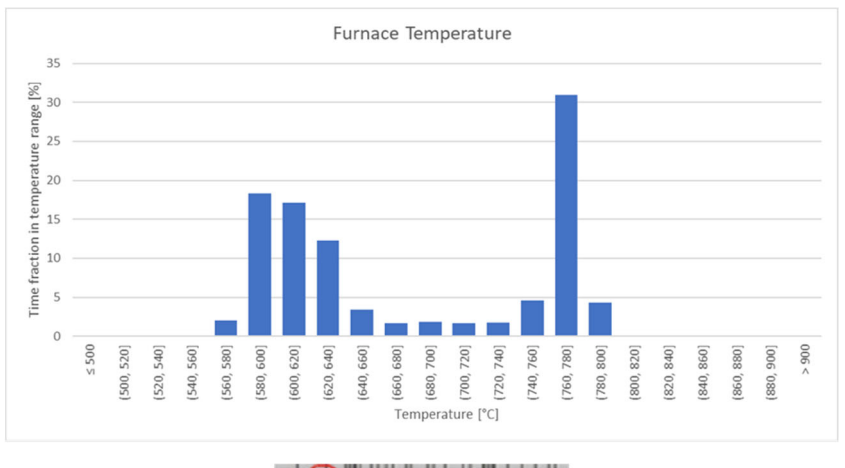


Figure 31: Diagram showing the flue gas temperature after the tertiary superheater during the first deposit test in the ASV06 boiler. The schematic shows the position at which the temperature was measured.



Figure 32: Diagram showing the boiler load during the second deposit test in the ASV06 boiler.





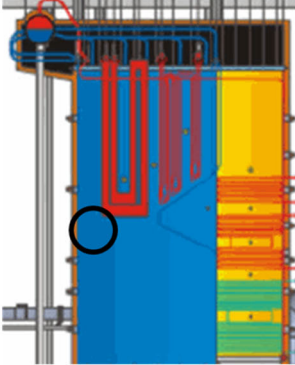


Figure 33: Diagram showing the furnace temperature during the second deposit test in the ASV06 boiler. The schematic shows the position at which the temperature was measured.



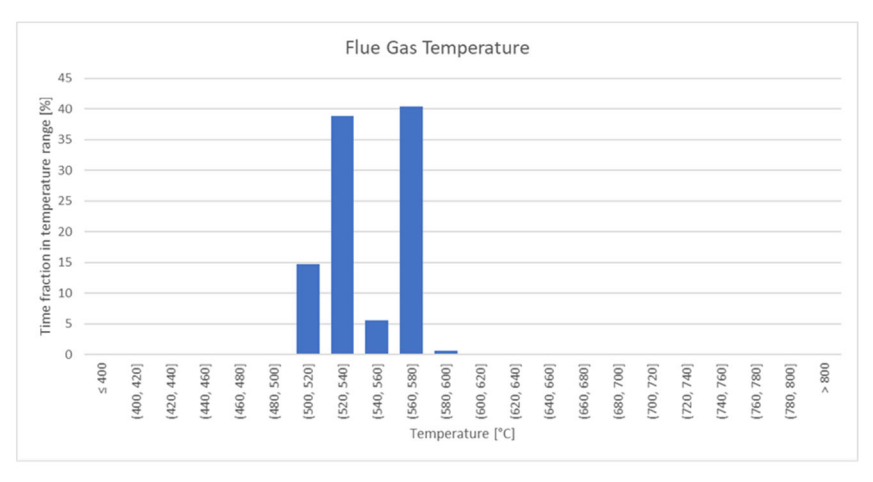


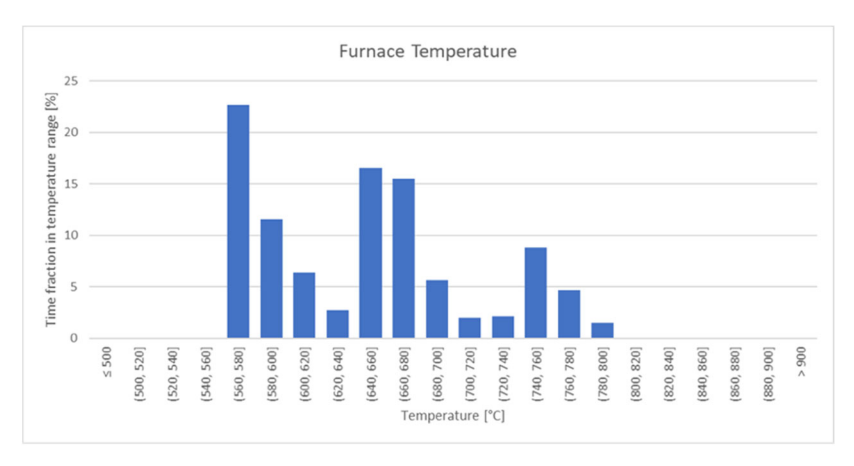


Figure 34: Diagram showing the flue gas temperature after the tertiary superheater during the second deposit test in the ASV06 boiler. The schematic shows the position at which the temperature was measured.



 $\textbf{Figure 35:} \ \ \text{Diagram showing the boiler load during the third deposit test in the ASV06 boiler.}$





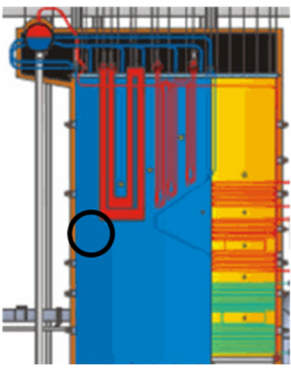
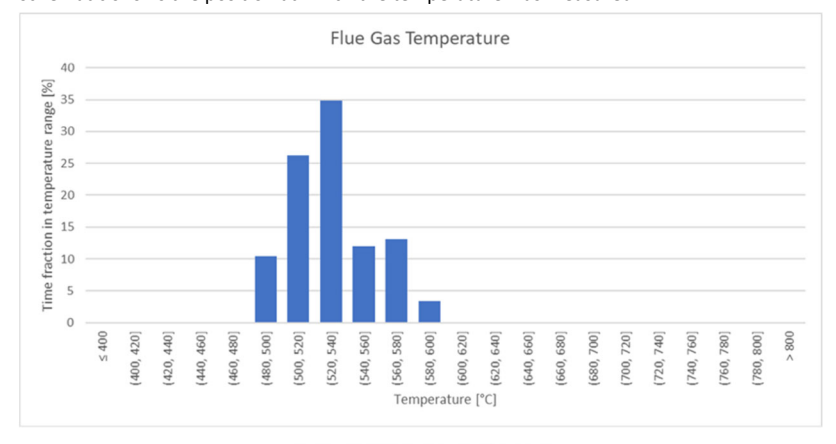


Figure 36: Diagram showing the furnace temperature during the third deposit test in the ASV06 boiler. The schematic shows the position at which the temperature was measured.



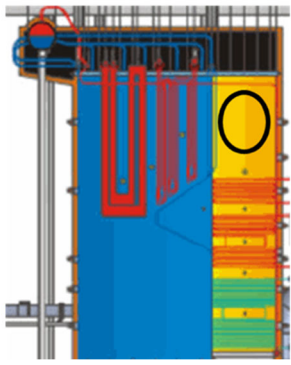


Figure 37: Diagram showing the flue gas temperature after the tertiary superheater during the third deposit test in the ASV06 boiler. The schematic shows the position at which the temperature was measured.



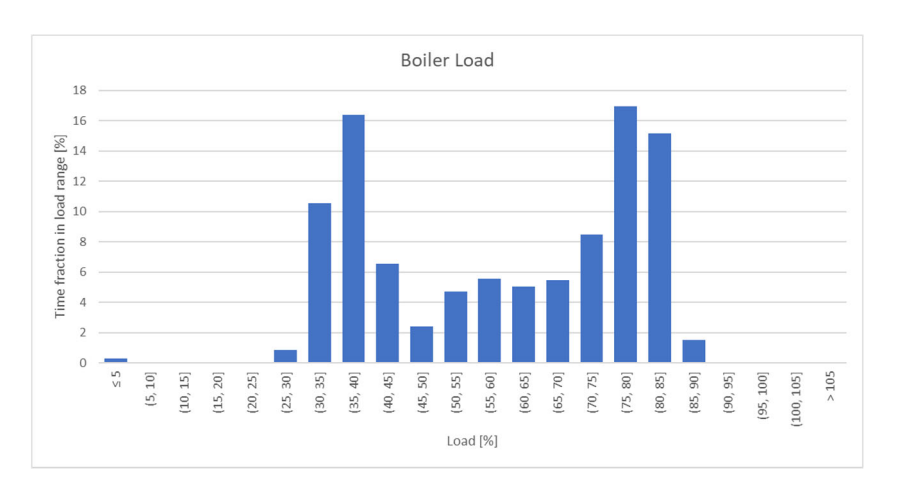
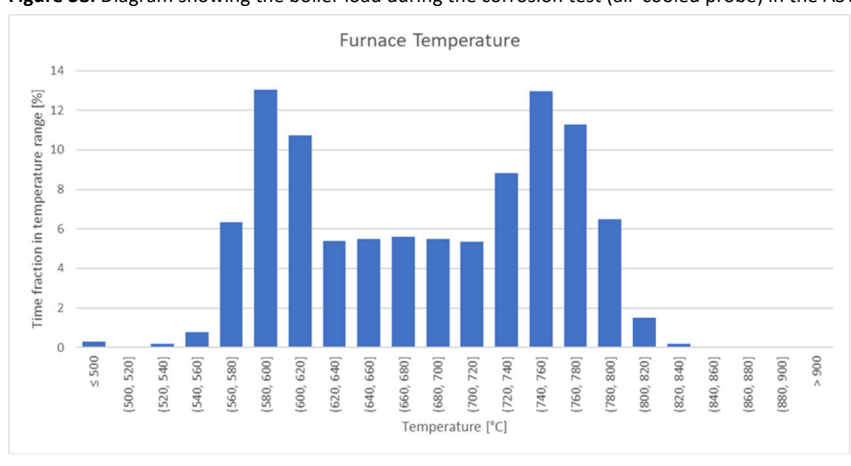


Figure 38: Diagram showing the boiler load during the corrosion test (air-cooled probe) in the ASV06 boiler.



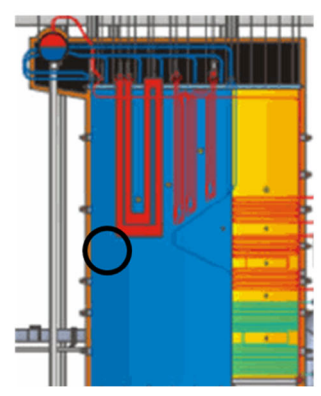


Figure 39: Diagram showing the furnace temperature during the corrosion test (air-cooled probe) in the ASV06 boiler. The schematic shows the position at which the temperature was measured.



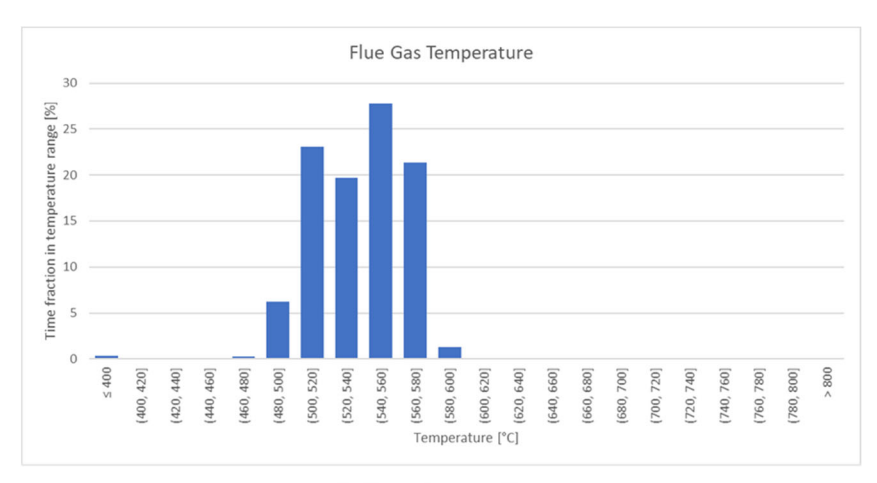




Figure 40: Diagram showing the flue gas temperature after the tertiary superheater during the corrosion test (air-cooled probe) in the ASV06 boiler. The schematic shows the position at which the temperature was measured.

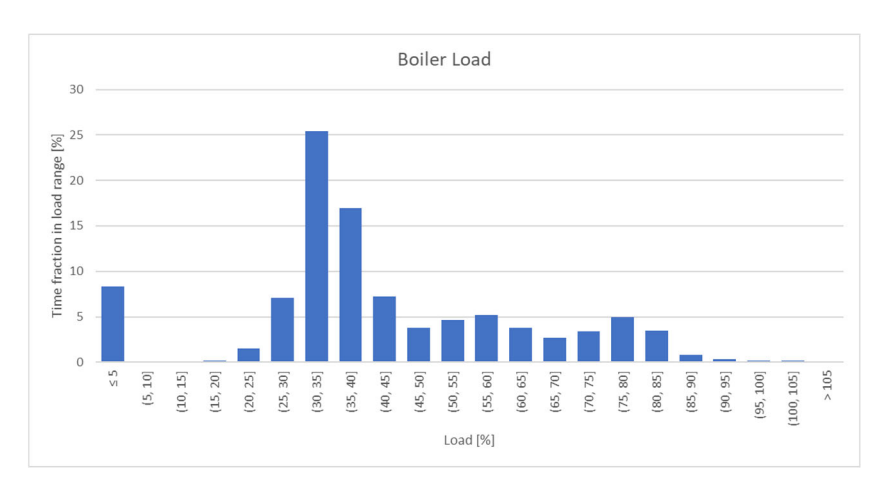
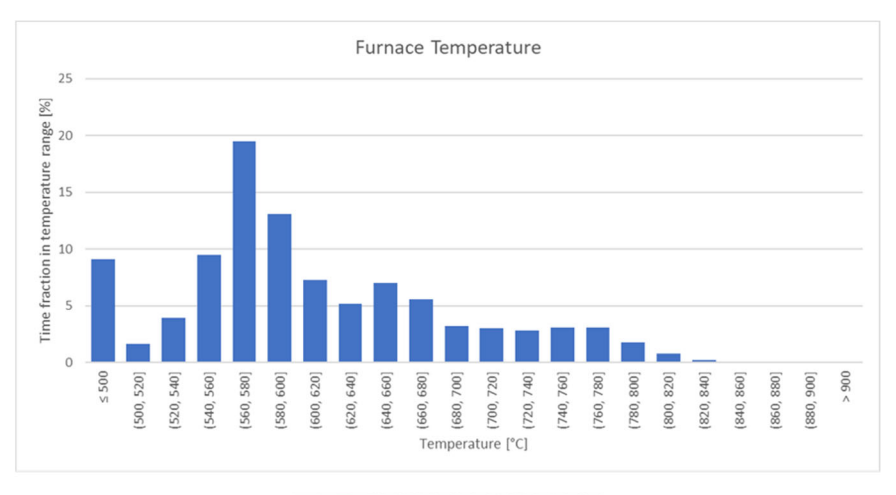


Figure 41: Diagram showing the boiler load during the period between the first fire and the planned maintenance outage (related to fixed installed samples) in the ASV06 boiler.





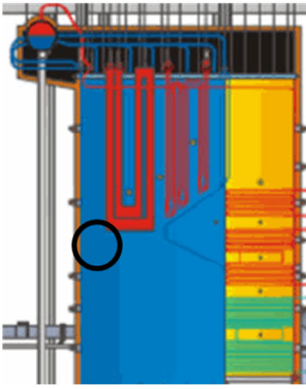
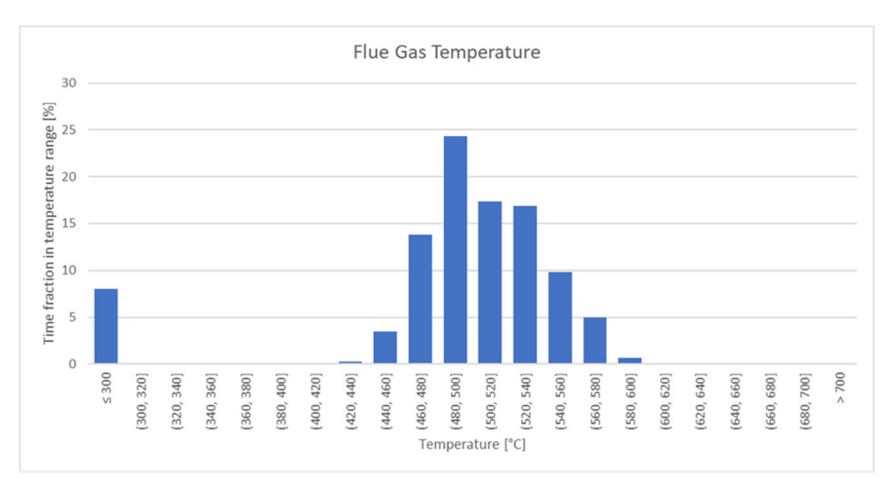


Figure 42: Diagram showing the furnace temperature during the period between the first fire and the planned maintenance outage (related to fixed installed samples) in the ASV06 boiler. The schematic shows the position at which the temperature was measured.





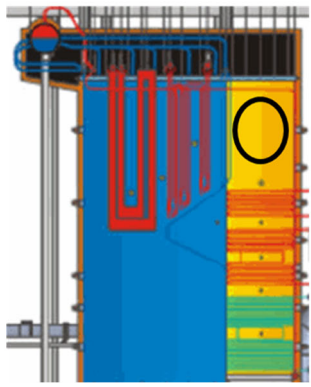


Figure 43: Diagram showing the flue gas temperature after the tertiary superheater during the period between the first fire and the planned maintenance outage (related to fixed installed samples) in the ASV06 boiler. The schematic shows the position at which the temperature was measured.

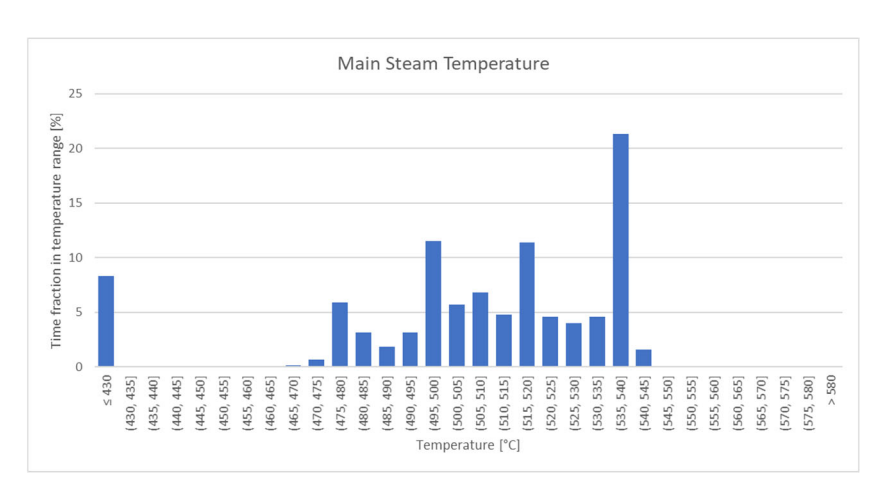


Figure 44: Diagram showing the main steam temperature during the period between the first fire and the planned maintenance outage (related to fixed installed samples) in the ASV06 boiler.



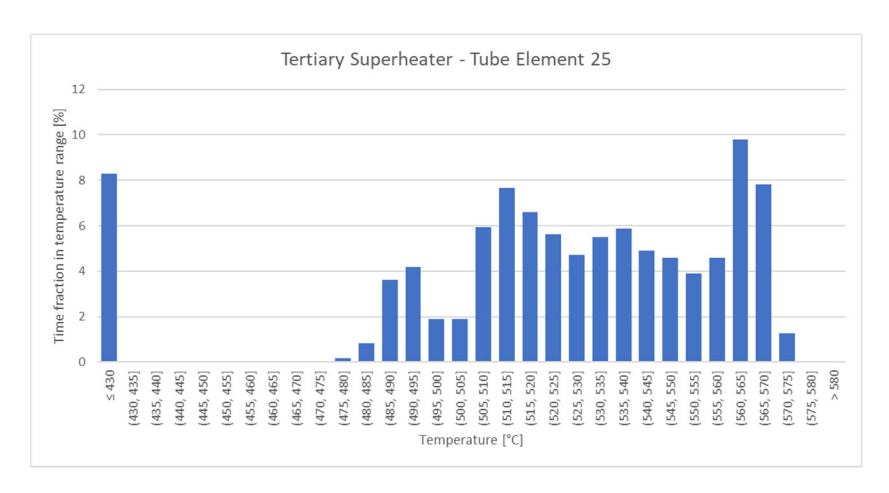


Figure 45: Diagram showing the steam temperature in tube element 25 of the tertiary superheaer during the period between the first fire and the planned maintenance outage (related to fixed installed samples) in the ASV06 boiler.

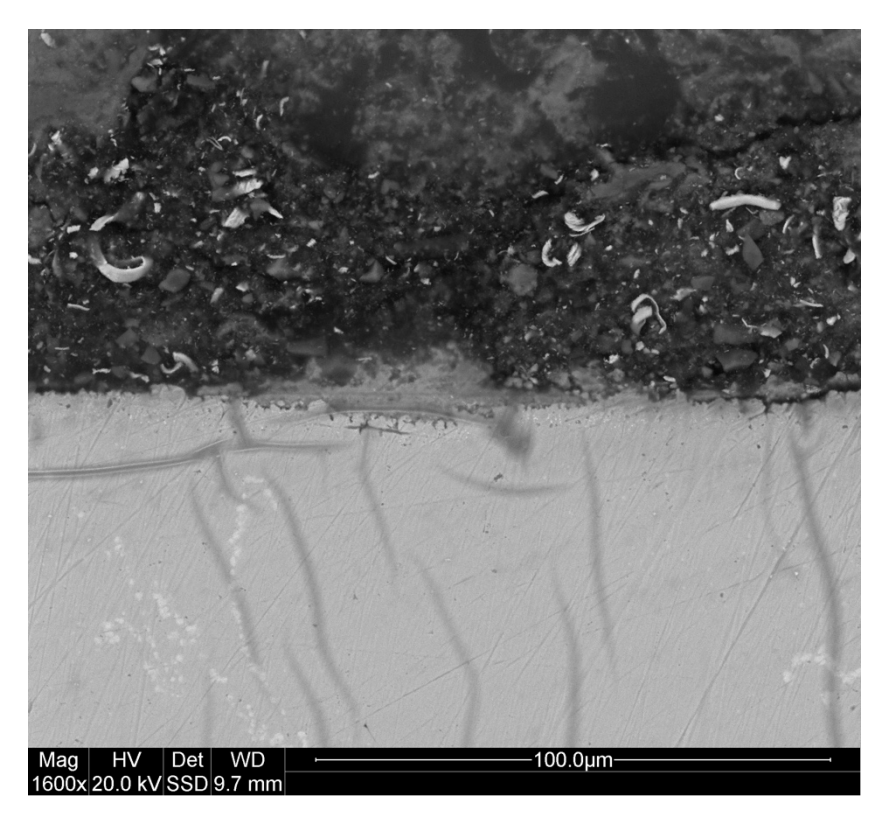


Figure 46: SEM-BSE image of Sanicro 25 after the long-term probe exposure at 600 °C.



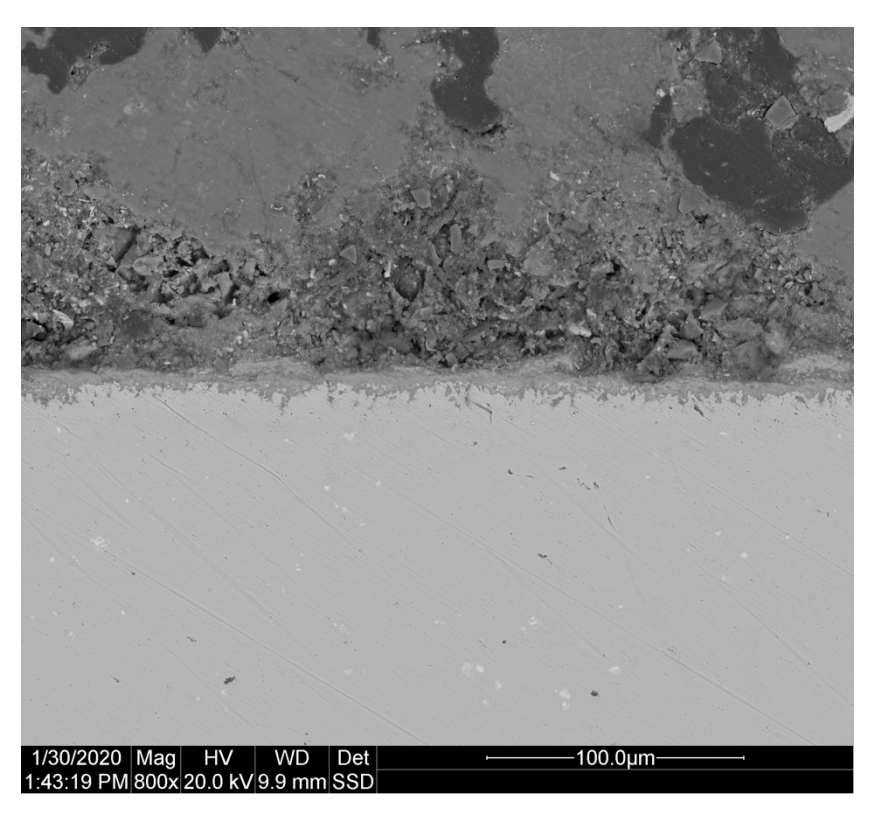


Figure 47: SEM-BSE image of 310HCbN after the short-term probe exposure at a position with high flue gas temperature and a material temperature of 700 $^{\circ}$ C.

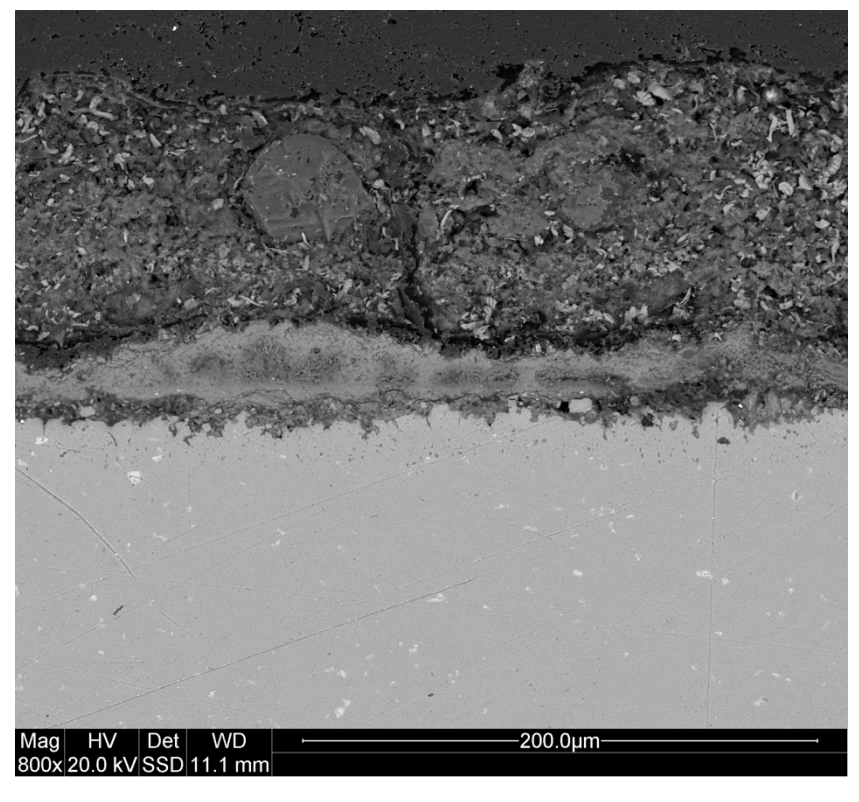


Figure 48: SEM-BSE image of 347H after the long-term probe exposure at a material temperature of 700 °C.



INCREASED FLEXIBILITY AND POWER PRODUCTION FROM BIOMASS THROUGH MATERIAL DEVELOPMENT AND CORROSION PREDICTION

With the goal to increase the efficiency and predictability/flexibility of power generation from biomass, this project has analyzed material development and oxidation simulations, through a combination of lab investigations, probe exposures as well as fixed installed material in a commercial boiler. The lab results show for example the potential in material development/selection to increase the efficiency in power generation from biomass through higher material temperatures.

Thermodynamic/kinetic calculations were performed to investigate the possibility to provide predictions of the corrosion rates in laboratory - probe - fixed installed materials. The strategy was based on the formation or chromia, alumina and iron oxide with input from the literature/lab/probe/fixed installed samples to optimize and confirm the accuracy of the calculations. The strategy gave accurate calculated oxide thicknesses in some cases, while the inaccuracy in other cases offered insights into necessary future improvements of the model, taking into consideration the formation of a healing layer after breakaway oxidation. This new knowledge may in addition aid not only in better predictions but also to develop/select corrosion resistant materials for harsh environments showing the potential in corrosion simulations/lifetime predictions.

Energiforsk is the Swedish Energy Research Centre – an industrially owned body dedicated to meeting the common energy challenges faced by industries, authorities and society. Our vision is to be hub of Swedish energy research and our mission is to make the world of energy smarter!

